Topics in Simulating Next-Generation Light Sources: Maps and Injectors

Chad Mitchell
P. Sprangle, J. Penano, D. Gordon, S. Gold, A. Ting[1], B. Hafizi[2]
[1]Naval Research Laboratory, Washington, DC; [2]Icarus Research

Alex Dragt
University of Maryland, College Park, MD

August 4, 2011

BERKELEY LAB
LAWRENCE BERKELEY NATIONAL LABORATORY

U.S. DEPARTMENT OF ENERGY

Overview

Two areas of interest for next-generation light-source design:

I. Realistic transfer maps (20-25 min)

- Surface methods for computing symplectic maps
- Method for general magnetic elements
- Benchmarks and applications

II. Injector simulation (20-25 min)

- Motivation: injectors for high-average power FELs
- Numerical challenges and benchmarks
- Simulation results and optimization studies

I. Realistic transfer maps

- A collection of methods has been developed that makes it possible to compute accurate high-order transfer maps for realistic beam-line elements to be used in charged-particle optics codes.

- Such methods use 3-d field data, provided on a grid by finite element modeling, to incorporate fringe field effects and nonlinear multipoles into a map description of beam dynamics.

- Once accurate transfer maps have been found for individual beam-line elements, one can determine all single-particle properties of the machine: dynamic aperture, tunes, chromaticities, anharmonicities, linear and nonlinear lattice functions, etc.

- Key is the use of surface data to compute interior data. Surface must enclose design trajectory and lie within all iron or other sources.

Lie-algebraic map methods

Given the phase space coordinates $\mathbf{z} = (q_1, p_1, q_2, p_2, q_3, p_3)$, we represent the dynamics of a single particle in each beamline element as a mapping:

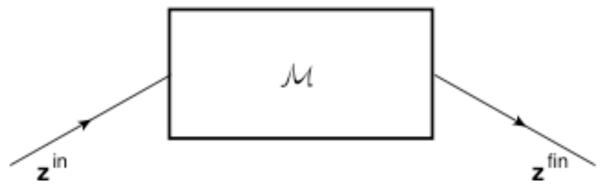

$$\mathrm{z}^{fin} = \mathcal{M}\mathrm{z}^{in}$$

Any analytic symplectic map which also maps the origin into itself can be written

$$\mathcal{M} = \mathcal{R}_2 e^{:f_3:} e^{:f_4:} e^{:f_5:} e^{:f_6:} \ldots$$

where $\mathcal{R}_2$ is the linear part of the map, represented by a matrix R_2 , and each f_m is a homogeneous polynomial of degree m .

Requires expansion about the design orbit $x^d(z)$, $p_x^d(z)$, $y^d(z)$, $p_y^d(z)$ etc. through the beamline element:

$$K = \sum_{s=1}^{S} h_s(z) K_s(\delta x, \delta p_x, \delta y, \delta p_y, \delta\tau, \delta p_\tau)$$

terms of degree 1 – design orbit
terms of degree 2 – R_2
terms of degree > 2 – f_m

Computing Accurate Maps

Suppose $\boldsymbol{E} = 0$. To obtain the $h_s(z)$, we need expressions of the form:

$$A_w(x,y,z) = \sum_{l=1}^{L} a_l^w(z) P_l(\delta x, \delta y) \quad \text{with} \quad w = x,y,z$$

Field data may be available on some 3-d mesh
- measured data (3d magnetic sensors)
- electromagnetic field solvers (eg., finite-element codes)

Numerical differentiation is unreliable for high-order $a_l^w(z)$ *due to amplification of noise.*

Noise spectrum ~ flat to $k = \pi / h$
Introduces weight to high spatial frequencies not present in true field B_y

$$\frac{\partial^n B_y}{\partial z^n} = F^{-1}\left[\underbrace{(ik)^n}_{\text{accentuates large spatial frequencies}} F[B_y] \right] \qquad \text{where} \qquad F[B_y] = \frac{1}{\sqrt{2\pi}} \int_{-\infty}^{\infty} e^{ikz} B_y(x,y,z)\, dz$$

Surface Fitting

• Fit measured/numerical field data to the boundary surface of a volume containing the design trajectory and excluding all iron or other sources (eg., a long "cylinder" in z with uniform cross-section).

• Interpolate inward using Maxwell's equations. In a source-free region, solutions are smooth (analytic) functions.

• Obtain an analytic representation of the interior vector potential ***A*** and its Taylor coefficients $a_w^l(z)$ in terms of surface data alone.

• Highly accurate and robust against numerical errors. Errors are damped as one moves away from the surface into the interior.

error appearing in derivative of order m $\leq \left(\frac{3m}{d}\right)^m \max_S |\delta B|$

d - distance of closest approach to surface

Accurate transfer maps can now be computed for realistic beamline elements of any machine, e.g. the ILC damping rings, using surface methods:

- Solenoids and multipoles -- circular cylinder (M. Venturini)
- RF cavities -- circular cylinder (D. Abell)
- Wiggler magnets -- elliptical / rectangular / circular cylinder (C. Mitchell)
- Bending dipoles -- bent box / bent cylinder (C. Mitchell, P. Walstrom)

use known Green's function

use new geometry-independent integration kernels

Consider the bent box.

The Bent Box and Other Geometries

• For straight-axis cylinder domains, only the normal component of $\boldsymbol{B}$ on the surface is needed to determine the interior vector potential.

• The circular, elliptical, and rectangular cylinder are special in that Laplace's equation is separable for these domains. This is not always possible.

• Surface data for general domains can again be used to fit interior data provided *both* $\boldsymbol{B}_{normal}$ and ψ are available on the surface. The magnetic vector potential in the interior can be determined by the integration of surface data against a *geometry-independent* kernel.

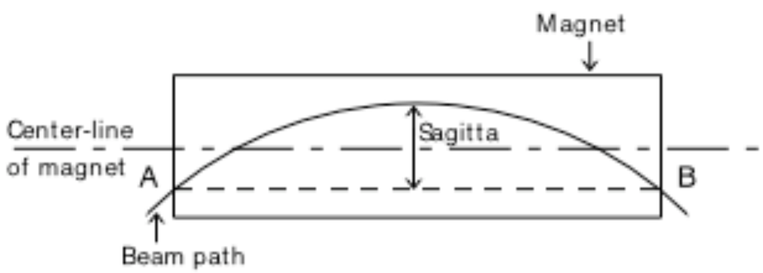

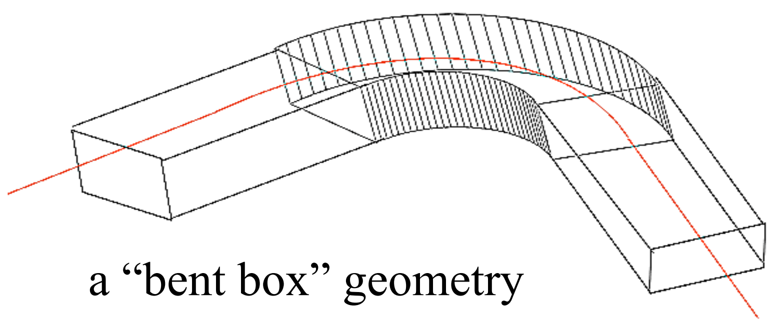

a "bent box" geometry

General Surfaces

Using the Helmholtz theorem and results relating to Dirac monopoles, we may write the interior vector potential in terms of surface data in the form

$$\boldsymbol{A} = \boldsymbol{A}^n + \boldsymbol{A}^t \quad \text{, where}$$

$$\boldsymbol{A}^n(\boldsymbol{r}) = \int_S [\boldsymbol{n}(\boldsymbol{r}')\cdot \boldsymbol{B}(\boldsymbol{r}')]\boldsymbol{G}^n(\boldsymbol{r};\boldsymbol{r}',\boldsymbol{m}(\boldsymbol{r}'))dS'$$

$$\boldsymbol{A}^t(\boldsymbol{r}) = \int_S \psi(r')\boldsymbol{G}^t(\boldsymbol{r};\boldsymbol{r}')dS' \quad .$$

The kernels are given by:

$$\boxed{\begin{aligned} \boldsymbol{G}^n(\boldsymbol{r};\boldsymbol{r}',\boldsymbol{m}) &= \frac{\boldsymbol{m}\times(\boldsymbol{r}-\boldsymbol{r}')}{4\pi\,|\boldsymbol{r}-\boldsymbol{r}'|\left[|\boldsymbol{r}-\boldsymbol{r}'|-\boldsymbol{m}\cdot(\boldsymbol{r}-\boldsymbol{r}')\right]} \\[2em] \boldsymbol{G}^t(\boldsymbol{r};\boldsymbol{r}') &= \frac{\boldsymbol{n}(\boldsymbol{r}')\times(\boldsymbol{r}-\boldsymbol{r}')}{4\pi\,|\boldsymbol{r}-\boldsymbol{r}'|^3} \end{aligned}}$$

normal component

tangential components

where $\boldsymbol{m}$ is a unit vector pointing along some line that does not intersect the interior (a Dirac string), and $\boldsymbol{n}$ is the unit normal to the surface at $\boldsymbol{r}'$.

The kernels $\boldsymbol{G}^n$ and $\boldsymbol{G}^t$ satisfy these properties:

- Each is analytic in the variables $\boldsymbol{r}$ at all points in the interior.
- $\nabla \times (\nabla \times \boldsymbol{G}^t(\boldsymbol{r};\boldsymbol{r}')) = \nabla \times (\nabla \times \boldsymbol{G}^n(\boldsymbol{r};\boldsymbol{r}',\boldsymbol{m})) = 0$ for all points $\boldsymbol{r}$ in the interior.
- $\nabla \cdot \boldsymbol{G}^t(\boldsymbol{r};\boldsymbol{r}') = \nabla \cdot \boldsymbol{G}^n(\boldsymbol{r};\boldsymbol{r}',\boldsymbol{m}) = 0$ for all points $\boldsymbol{r}$ in the interior.

As a result, the vector potential $\boldsymbol{A}$ is guaranteed to satisfy Maxwell's equations $\nabla \times (\nabla \times \boldsymbol{A}) = \nabla \times \boldsymbol{B} = 0$ and the Coulomb gauge condition $\nabla \cdot \boldsymbol{A} = 0$.

Given a point along the design orbit, we may construct a power series for $\boldsymbol{A}$ about $\boldsymbol{r}_d$ by integrating the surface data against the power series for the $\boldsymbol{G}$'s, term-by-term.

Each Taylor coefficient is obtained from a single surface integration.

This has been implemented numerically to compute coefficients a_l^w of the vector potential about any point on the design orbit.

Code accepts as input 3d data of the form $(\boldsymbol{B},\psi)$ on a mesh and will produce as output:

1) Vector potential $\boldsymbol{A}$ at any interior point (gauge specified by orientation of strings)
2) Taylor coefficients of $\boldsymbol{A}$ about any design point through degree N

which in turn are used to compute…

3) Interior field $\boldsymbol{B}$ at any point
4) Taylor coefficients of $\boldsymbol{B}$ about any point
5) $\nabla \cdot \boldsymbol{A}, \quad \nabla \times \boldsymbol{A}, \quad \nabla \cdot \boldsymbol{B}, \quad \nabla \times \boldsymbol{B}$

benchmark tools

Code produces interior fits that satisfy Maxwell's equations exactly even if the surface data is noisy and the required surface integrals are performed only approximately.

Transfer maps are then computed from the Taylor expansion of $\boldsymbol{A}$ along the design orbit.

Monopole Doublet Benchmark

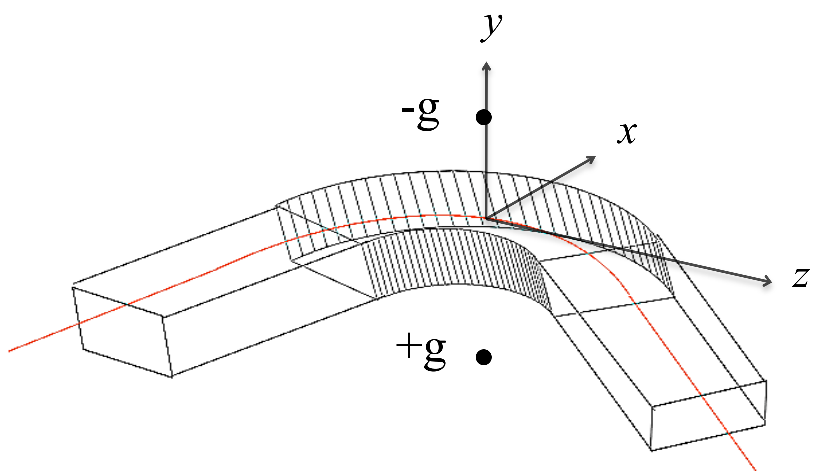

$g = 1$ T-cm^2, $a = 2.5$ cm

8.65 MeV positrons: 30 degree bend

Exactly soluble, numerically challenging test field.

- Magnetic field and its Taylor coefficients are known exactly.
- Vector potential and its Taylor coefficients are known exactly in one gauge.
- Integrate to obtain the reference trajectory and the map about the reference trajectory using 1) exact vector potential, 2) vector potential computed from surface data.

compared

Computed magnetic field

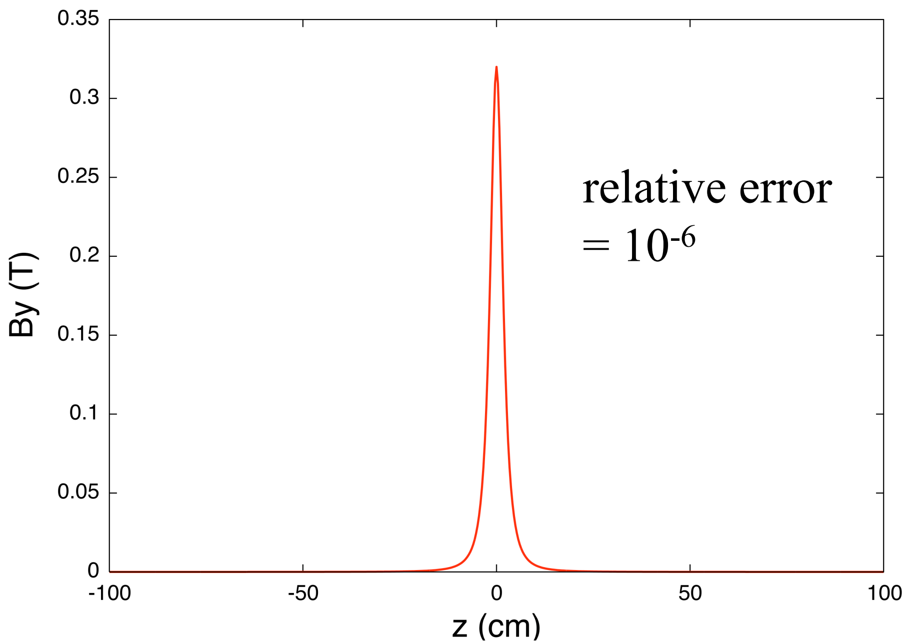

Computed vector potential

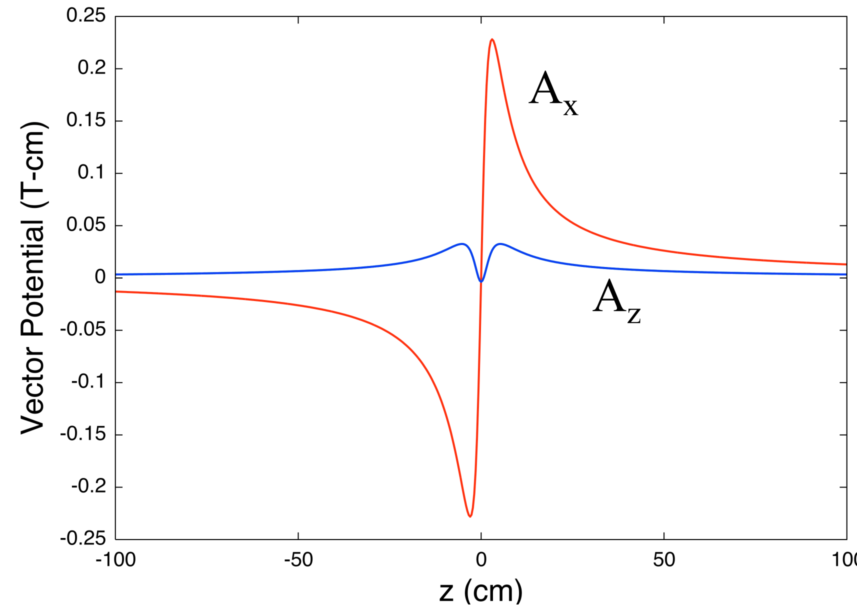

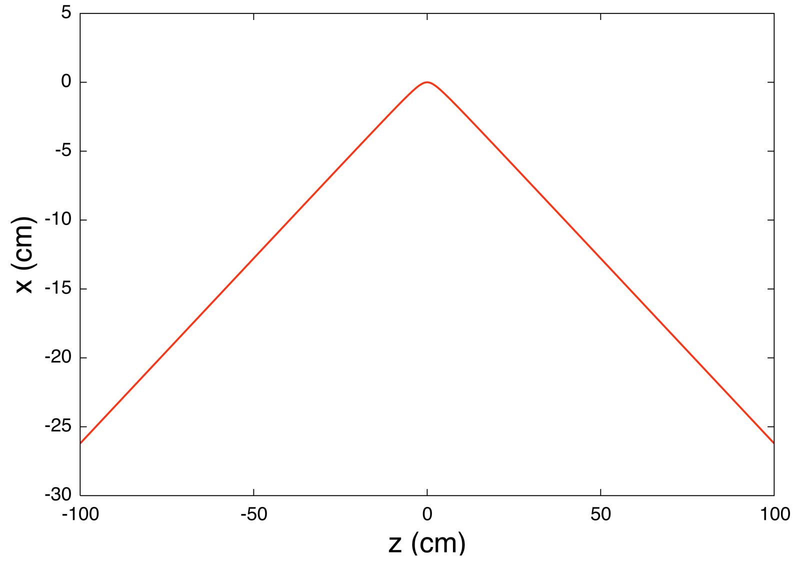

Reference trajectory

largest error in x,
relative to peak excursion,
is 5 x 10^{-7}

Field coefficients

worst error/peak ~ 10^{-4}
typical error < 10^{-5}

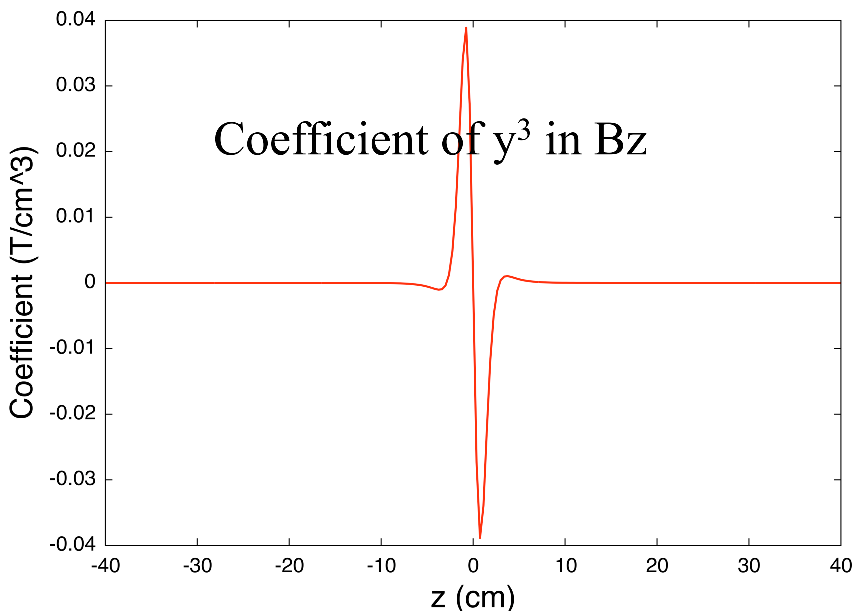

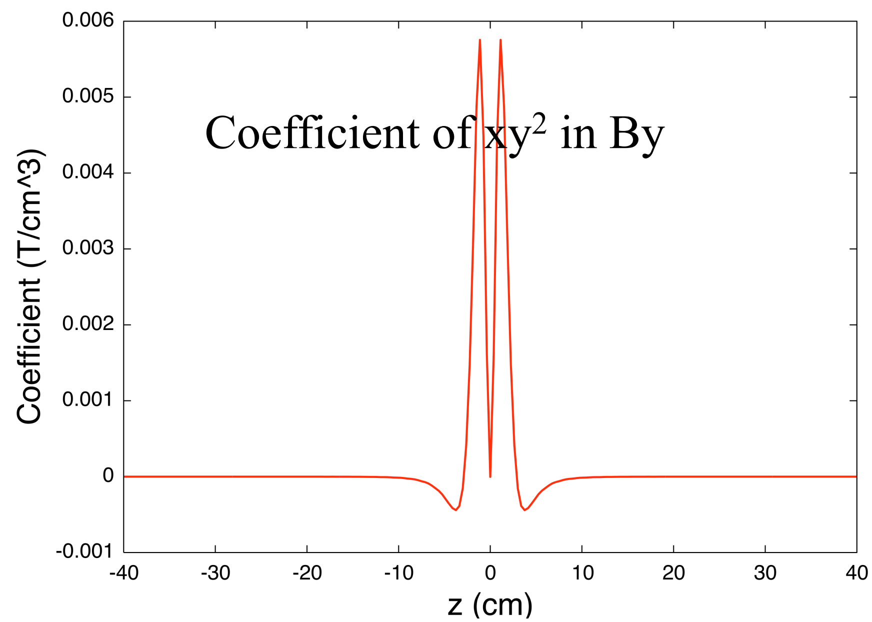

Comparison of Maps

Largest error in linear map and nonlinear generators through f_4 : $\sim 10^{-4}$

Error scales as Δ^4 for trajectories near the reference trajectory, as expected,

where $\Delta = \left\| z^{\text{in}} - z^{\text{in,ref}} \right\|$.

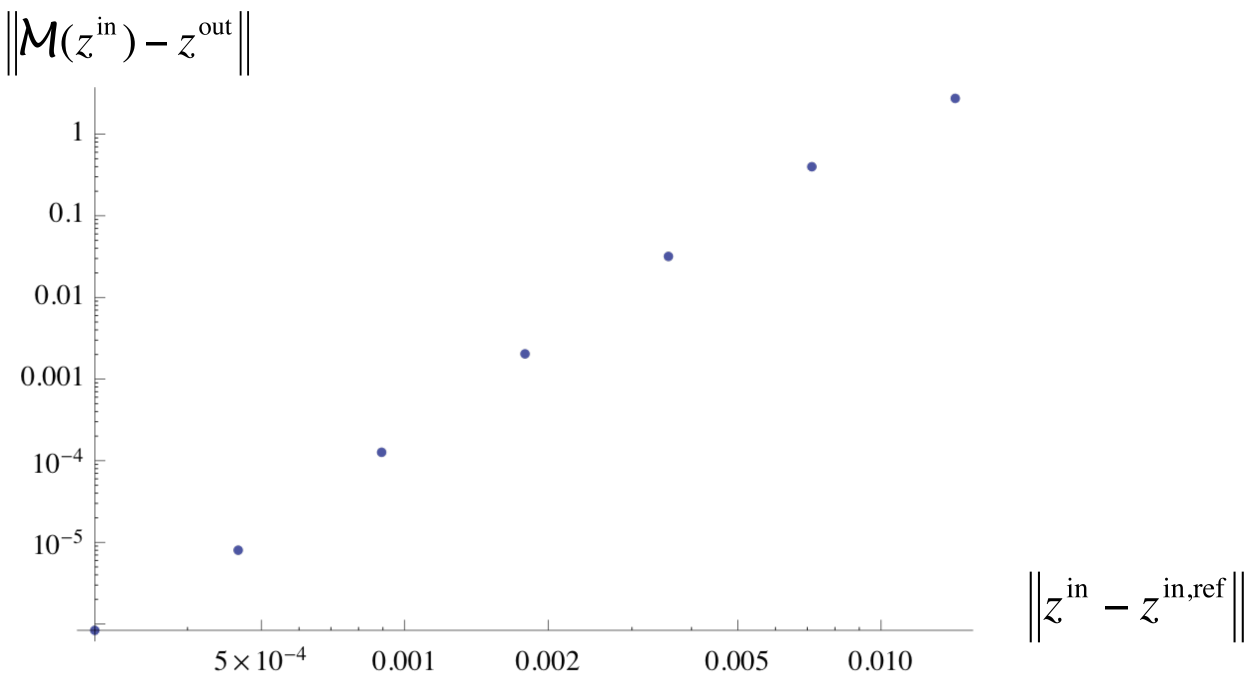

Fitting NSLS-II Dipole Data Using a Bent Box

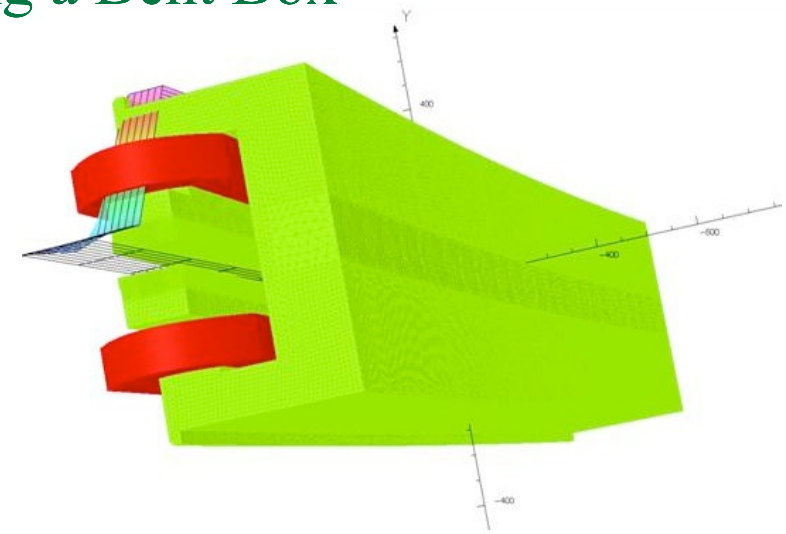

Data provided for the 35-mm gap Brookhaven dipole on the domain:
x in [-0.06, 0.06] m,
y in [-0.016, 0.016] m,
z in [-1.8, 1.8] m,
Spacing of mesh points h = 2 mm

The interior magnetic field was obtained and compared against the numerically computed values provided at the interior mesh points.

The three components of vector potential and their Taylor coefficients were computed through 4th degree to obtain a design orbit and the 3rd order transfer map about that orbit.

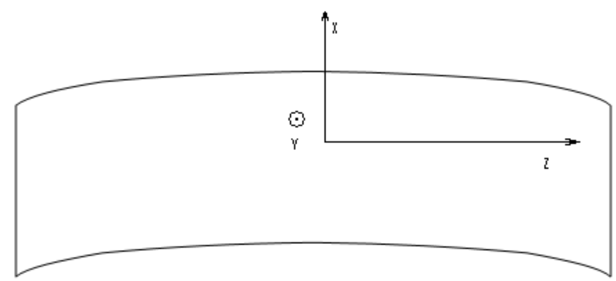

3 GeV electrons: 6 degree bend

Fit to the NSLS-II Dipole Field Using a Bent Box

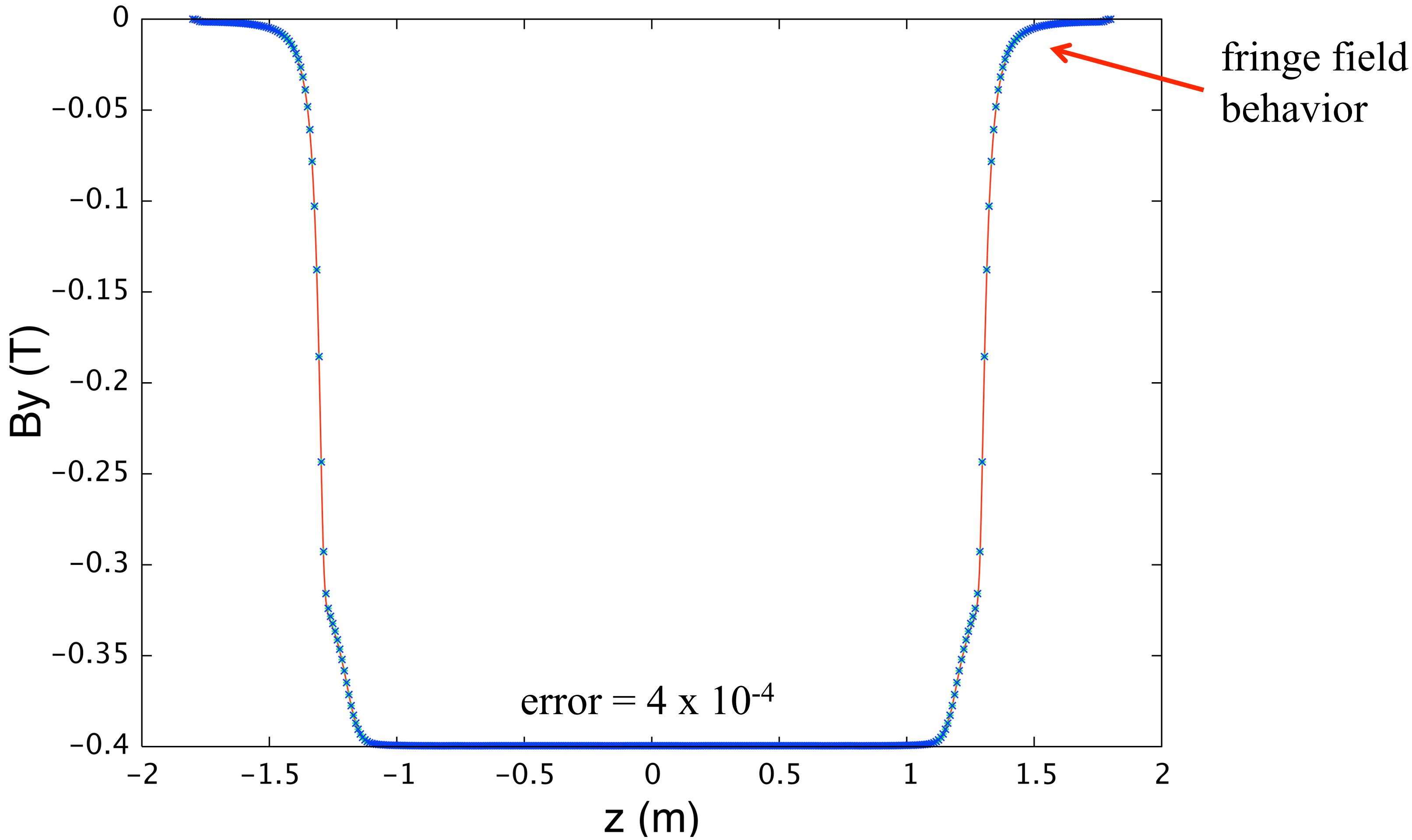

Fit to vertical field B_y
at x=0 cm, y=0.2 cm.

Fit to the NSLS-II Dipole Field Using a Bent Box

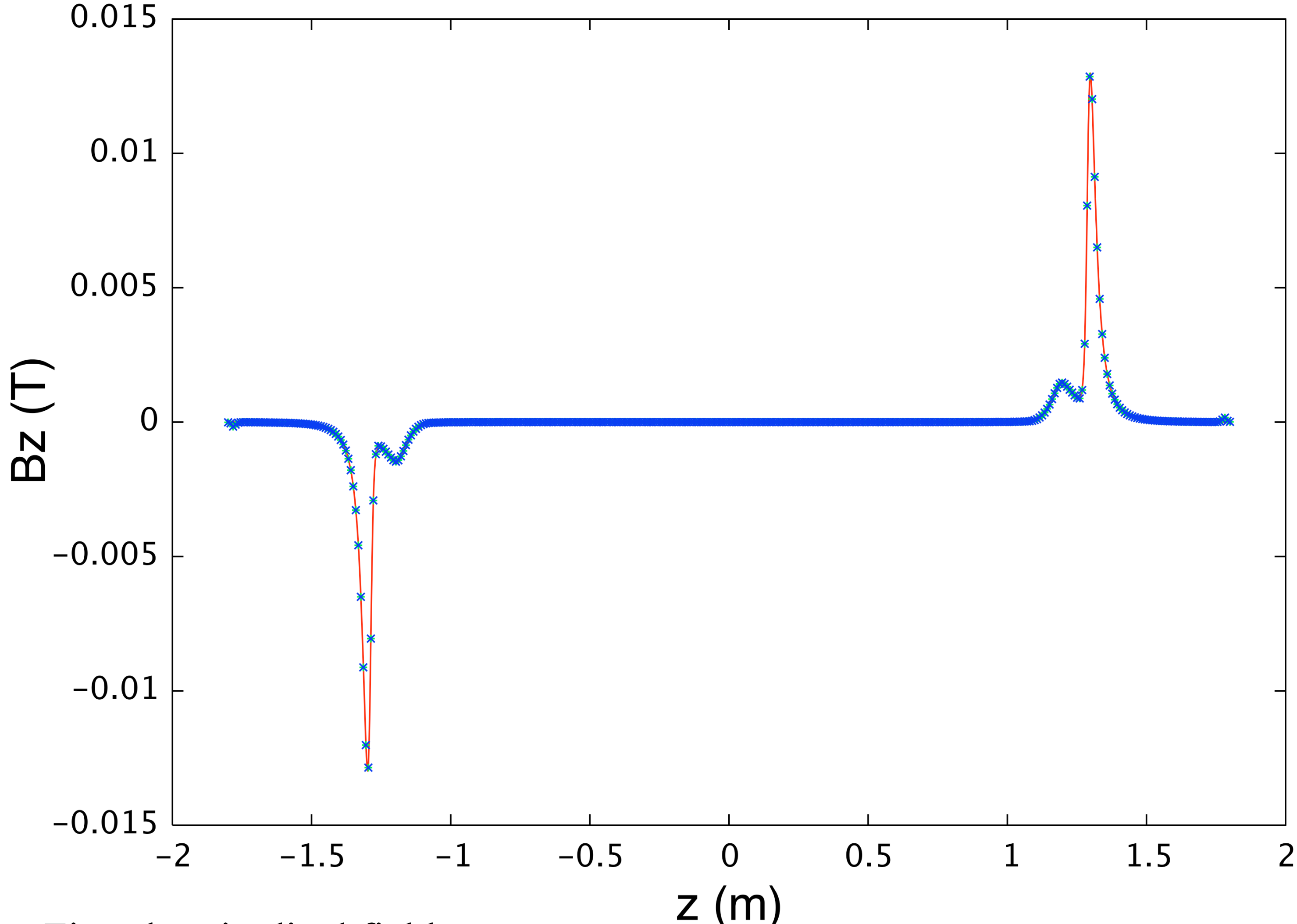

error in peak field $= 3 \times 10^{-4}$

Fit to longitudinal field B_z at x=0 cm, y=0.2 cm.

Fit to the NSLS-II Dipole Field Using a Bent Box

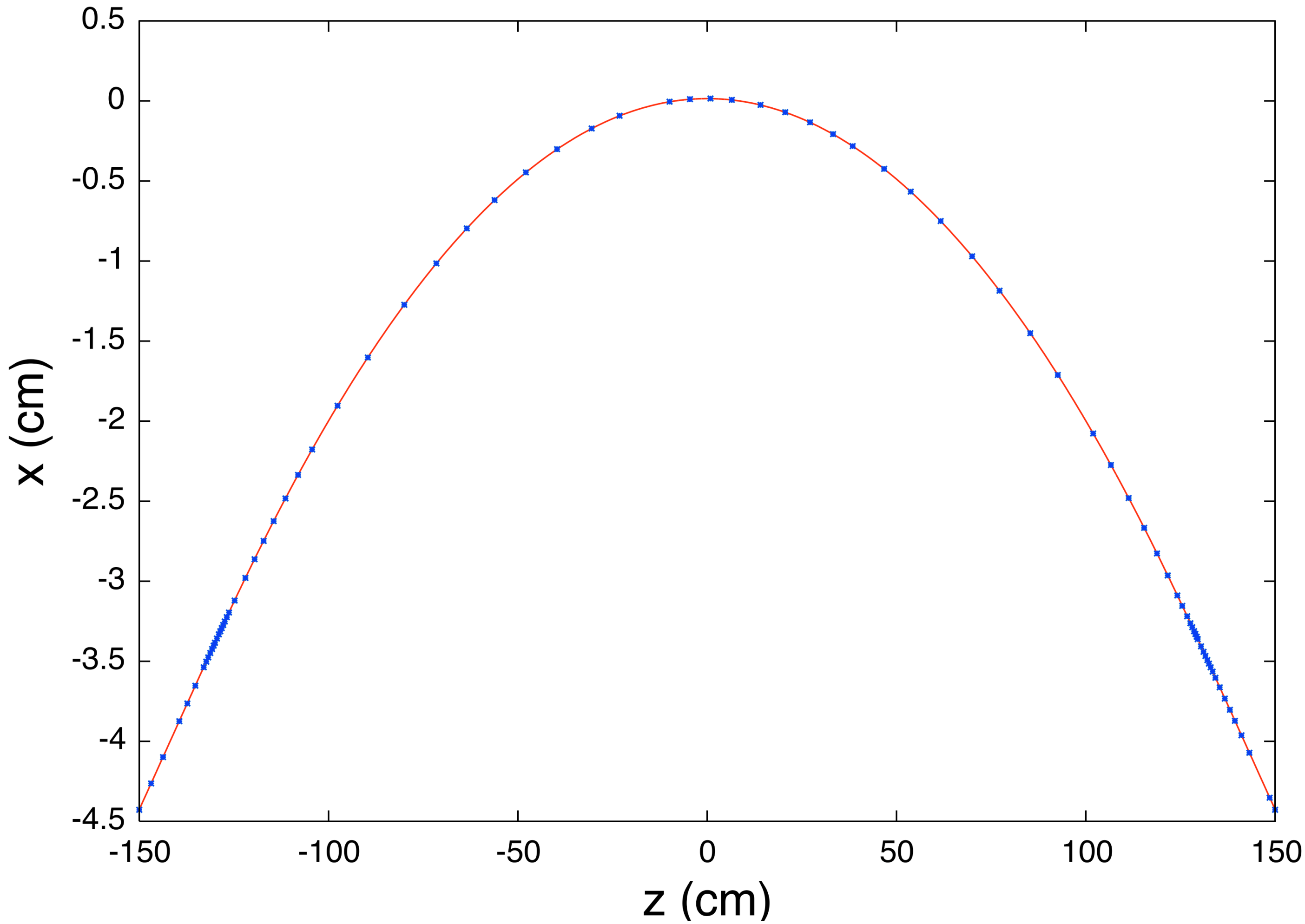

Reference trajectory

Advantages of surface fitting

Surface methods have many advantages over on-axis or midplane fitting:

- Maxwell equations are exactly satisfied.
- Error is globally controlled. The error must take all extrema on the boundary, where we have done a controlled fit.
- Careful benchmarking against analytic results for arrays of magnetic monopoles.
- Surface integration is *smoothing*. Insensitivity to noise improves with increased distance from the surface.

  For example, in a magnetic monopole doublet test case, adding a 1% surface noise produced only a 0.01% change in the computed transfer map.

These techniques have been applied to compute maps for NSLS-II dipoles and ILC damping ring wigglers.

II. Injectors for High-Average Power FELs

- High average power FELs require a train of high quality bunches with high average current. These requirements place stringent constraints on the electron injector portion of the FEL.

- Photocathode guns are capable of generating short, high-quality and high-charge electron bunches and are employed in the majority of FELs. However, photocathodes face limitations when operated at high-average powers.

- Thermionic guns have demonstrated long life-time operation and high current densities. The use of an RF-gated grid may allow one to achieve high repetition rates and ~1 nC bunches using thermionic cathodes.

- A numerical and experimental program is in place to investigate RF-gated emission using an IOT thermionic injector gun.

Electron Beam Quality Requirements

- FEL beam quality requirement entering wiggler $\Delta\beta_z << \lambda / 2\, L_{eff}$

$$\frac{\Delta E_{total}}{E} = \frac{1}{2}\frac{\varepsilon_{n,\perp}^2}{r_b^2} + \frac{\varepsilon_{n,z}}{E_b\,\tau_b} + \frac{\pi^2\, a_w^2}{2}\frac{r_b^2}{\lambda_w^2} << \frac{\lambda_w(1 + a_w^2/2)}{4\,L_{eff}} \sim 3\text{–}5\%$$

L_{eff} – gain length (amplifier) or wiggler length (oscillator)
a_w – wiggler parameter
λ_w – wiggler period
r_b – bunch radius

- Typical parameters for a beam entering MW-class FEL wiggler

$\varepsilon_{n,\perp} < 20\,\text{mm}-\text{mrad}$, $\varepsilon_{n,z} = < 200\,\text{keV}-\text{psec}$, $\mathrm{r_b} < 0.5\,\text{mm}$, $\tau_b < 3\,\text{psec}$

$I_{peak} \sim 500\,A$, $E_b = 80\,\text{MeV}$, $a_w^2 = 2$, $\lambda_w = 3\,\text{cm}$

High-Average Current Injector

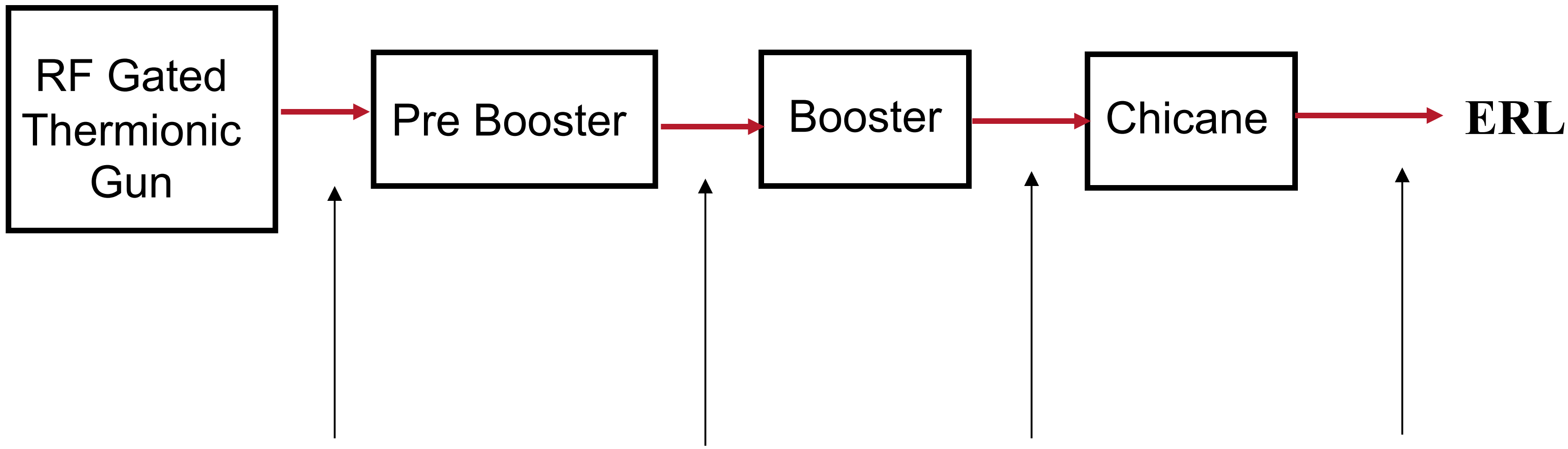

$E_b \sim 30-100\,\mathrm{keV}$

$q\,N_b \sim 1\,\mathrm{nC}$

$\langle I_b \rangle \sim 1\,\mathrm{A}$

$\tau_b \sim 40-50\,\mathrm{psec\,(rms)}$

$\varepsilon_{n,\perp} \sim 5-10\,\mathrm{mm-mrad}$

$\varepsilon_{n,z} \sim 30\ \mathrm{keV-psec}$

$E_b \sim 2\,\mathrm{MeV}$

$E_b \sim 5-8\,\mathrm{MeV}$

$\tau_b \sim 5-10\,\mathrm{psec\,(rms)}$

$\varepsilon_{n,\perp} \sim 10-15\,\mathrm{mm-mrad}$

$\varepsilon_{n,z} \sim 100\ \mathrm{keV-psec}$

700 MHz

RF Gated Gridded Thermionic Injector

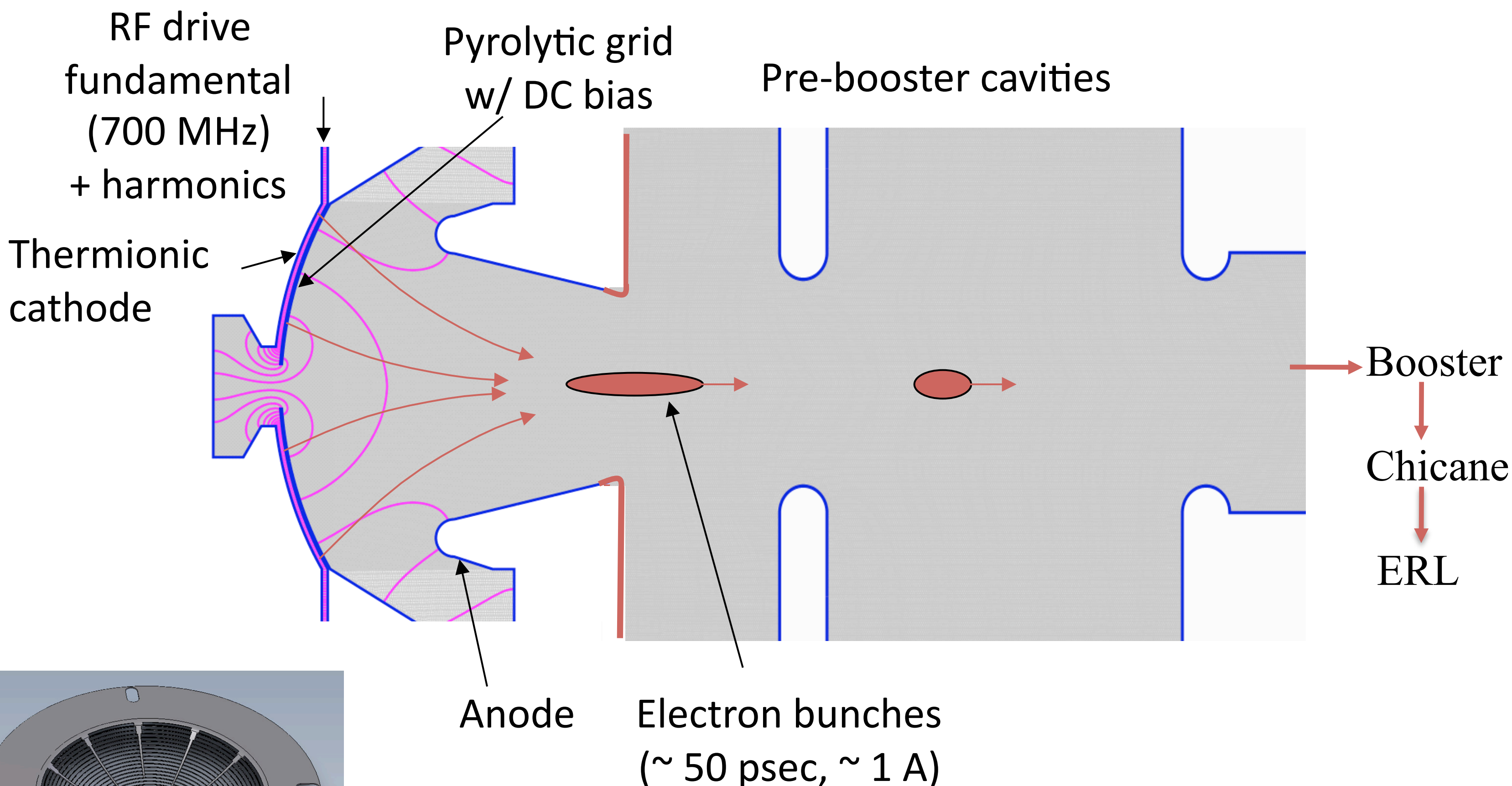

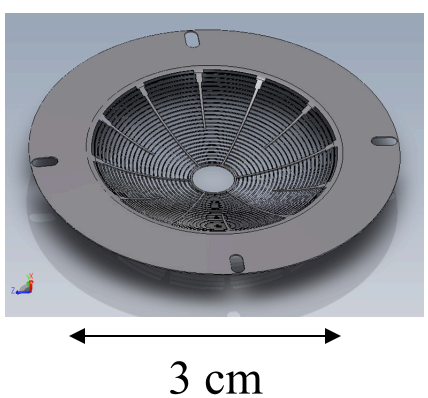

grid wire separation 450 μm
grid wire radius 30 μm

Emission occurs only during the portion of RF phase when $E_z < 0$ in the gap, providing longitudinal bunching.

The addition of the higher harmonics provides shorter bunches.

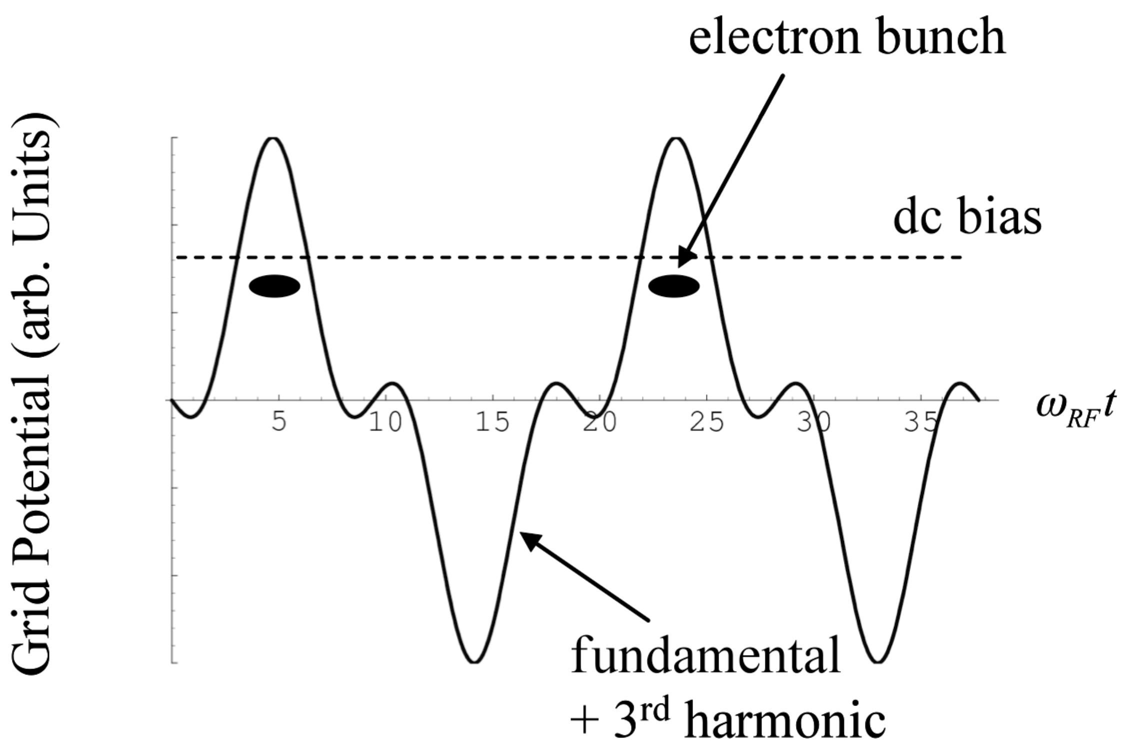

Numerical Challenges

- Proper modeling of thermionic emission from the cathode.
- Large difference in spatial scales between the cathode-grid gap (250 μm) and the main body of the gun (5 cm).
- Complex geometry of the conducting surfaces, especially the grid wires.
- Absence of azimuthal symmetry suggests 3d simulation may be necessary.
- Presence of an externally driven rf field. Fully electromagnetic simulation?

RF wavelength/cathode radius = 30

MICHELLE (NRL, SAIC, AWR Corp.)

- *Originally designed* for treatment of (static) gridded electron guns, collectors.
- Correct boundary conditions are enforced (image charges present on all conducting surfaces)
- Contains a fully 3d, time-dependent particle-in-cell code.
- Can read-in a 3d CAD model of the gun geometry.
- Unstructured meshing allows fine-scale resolution of grid wires.
- ANALYST package includes a 3d solver for time-dependent, driven RF fields.

Evaluating MICHELLE Simulation of Injector Gun

- **Model**
  Geometry – SolidWorks volume, 2d vs 3d effects, symmetry
  Boundary conditions

- **Numerical convergence**
  Mesh quality – element size/gap << 1, element size/Debye length < 1
  Timestep – timestep/transit time << 1, element crossings/timestep < 1, timestep*plasma freq < 1
  Number of particles – typically 10^5-10^6

- **Algorithm**
  Emission models
  Integration of the equations of motion
  Finite-element field solver
  Particle and field weighting

- **Diagnostics**
  Current
  Bunch size
  Emittance

2d Gun Modeling in ANALYST

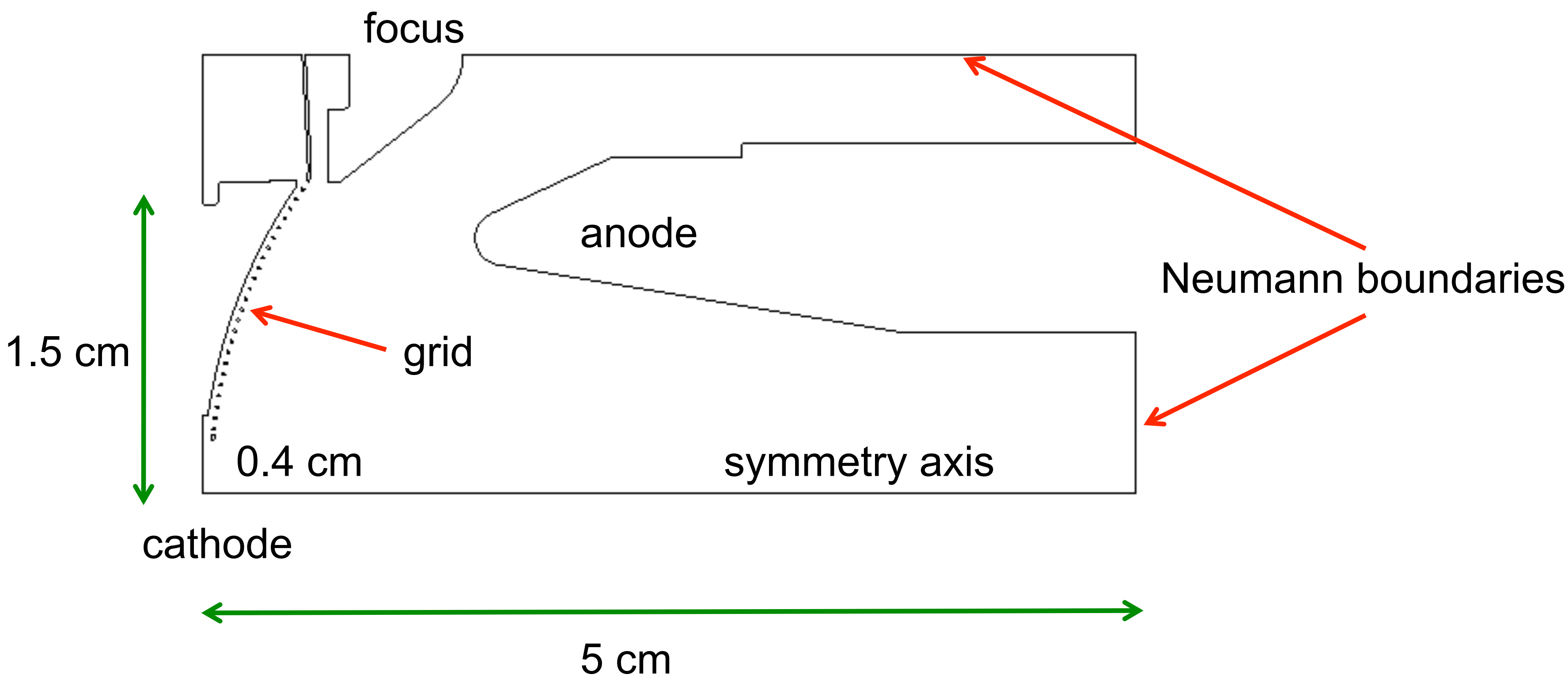

Numerical Convergence

Length scales – cathode-grid gap ~ 250 μm
cathode radius ~ 1.5 cm
gun length ~ 5 cm

L cathode-grid gap

Time scales – transit time across the gap ~ 90 psec
transit time across the gun ~ 1.2 nsec
RF period ~ 1.4 nsec

$$T_{CL} = 3L\sqrt{m/2eV_0}$$

Charge scales – maximum charge supported in the gap ~ 2 nC
bunch charge ~ 1 nC

$$Q_{CL} = \frac{4}{3}\varepsilon_0 V_0 / L$$

Resolution of the cathode-grid region:

transit time / timestep > 100   gap distance / mesh size ≈ 20
element crossings / timestep ≤ 1

Mesh Quality

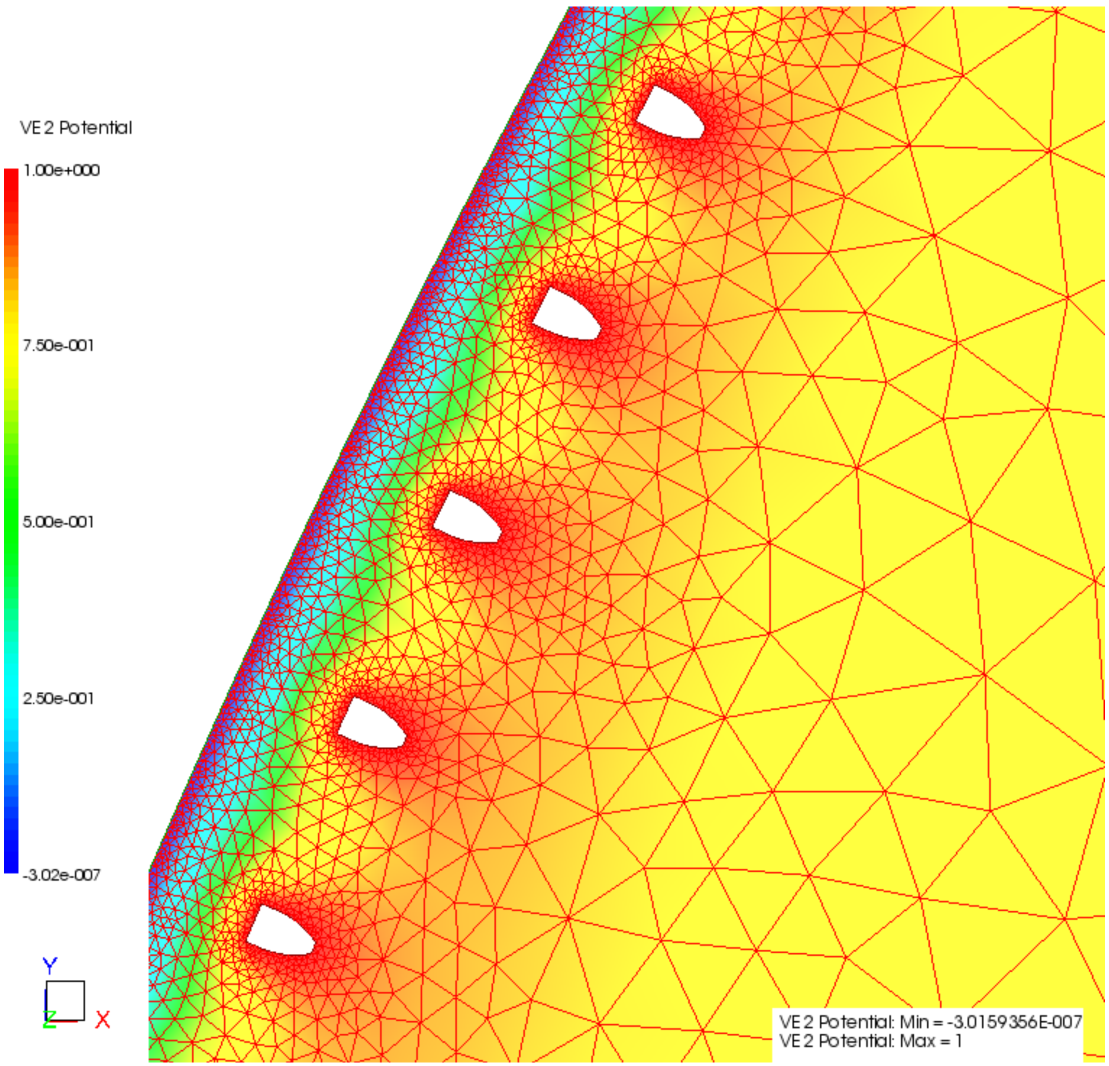

unstructured meshing: resolution of the cathode-grid region

~ 15 element crossings between cathode and grid

A 2d steady-state run is performed for a fixed anode potential (35 kV). Taking ½ the mesh element size results in a change in both the emitted current and the emittance of < 1%.

Emission Algorithm

At the cathode, a fixed number of particles are launched from each element face. Models of current vs voltage are used to determine how charge is deposited on the mesh.

- Space-charge limited (Child-Langmuir)

$$J_{CL} = \frac{4}{9}\varepsilon_0(2\eta)^{1/2}\frac{V^{3/2}}{d^2}$$

V – potential difference
d – gap distance
η – charge/mass ratio

- Temperature limited (Richardson-Dushman-Schottky)

$$J_{RD} = A_0 T^2 \exp[-q(\phi_W - \phi_S)/kT] \qquad \phi_S = \sqrt{\frac{q|E|}{4\pi\varepsilon_0}}$$

ϕ_W – work function
T – cathode temperature
E – field magnitude at cathode
A_0 – numerical constant

- Transition region (Longo-Vaughn)

$$\frac{1}{J_{LV}{}^{\alpha}} = \frac{1}{J_{CL}{}^{\alpha}} + \frac{1}{J_{RD}{}^{\alpha}}$$

exponent α characterizes how sharply transition occurs

Benchmarks of the Emission Model

Simulation of a plane diode (Child-Langmuir)

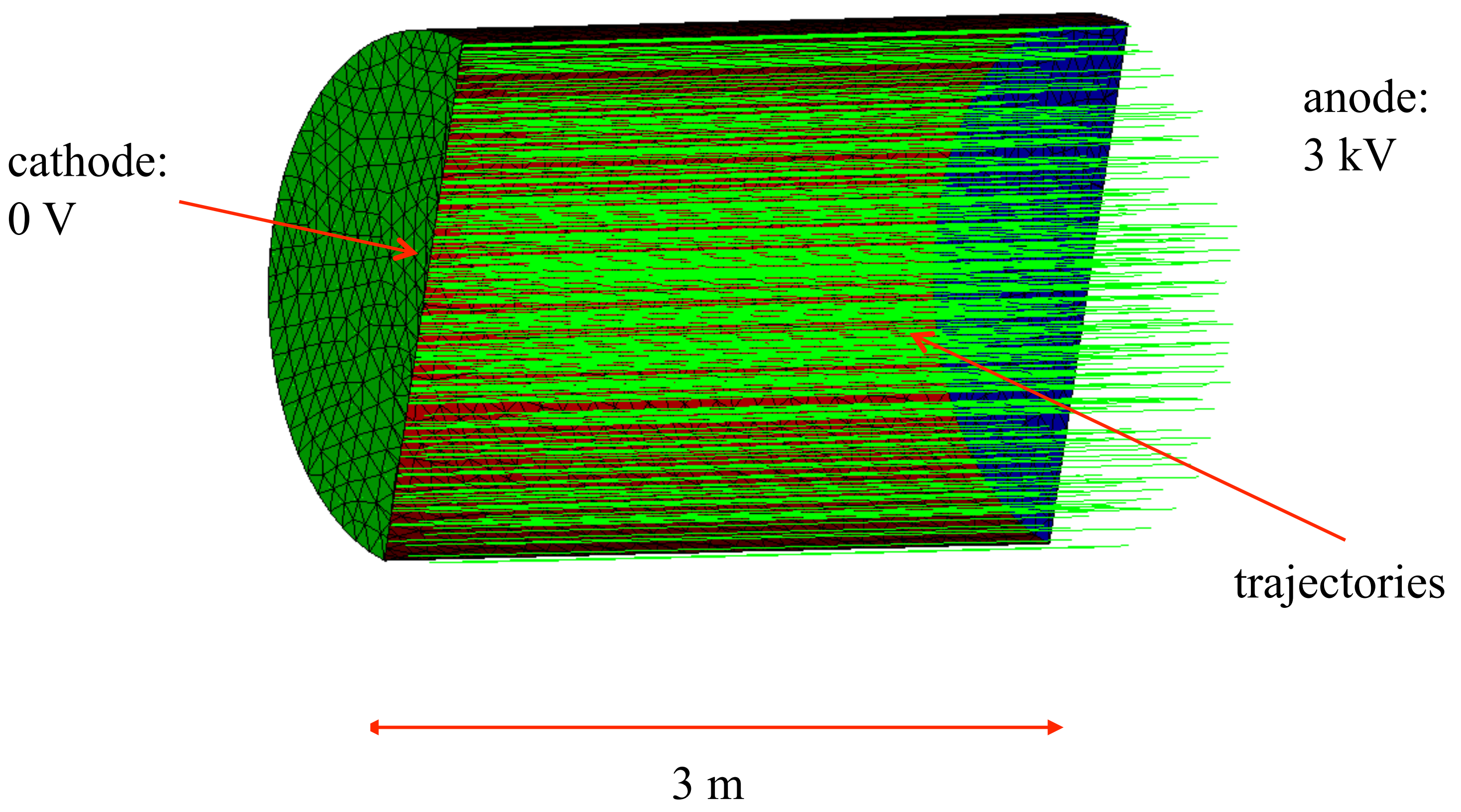

Child-Langmuir Benchmark

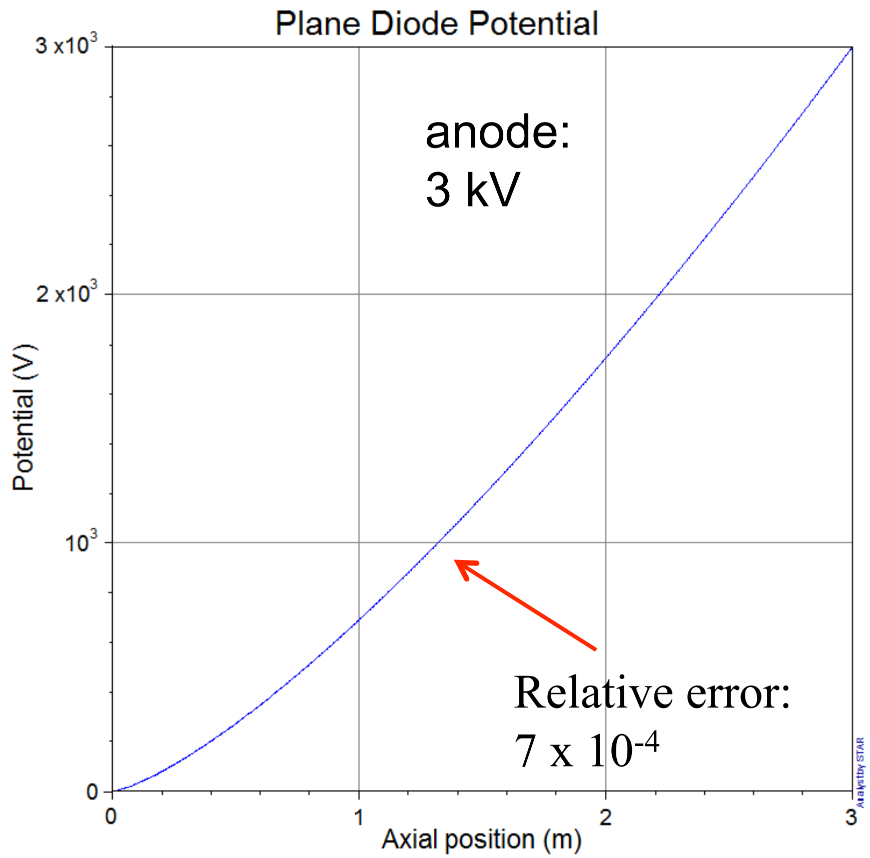

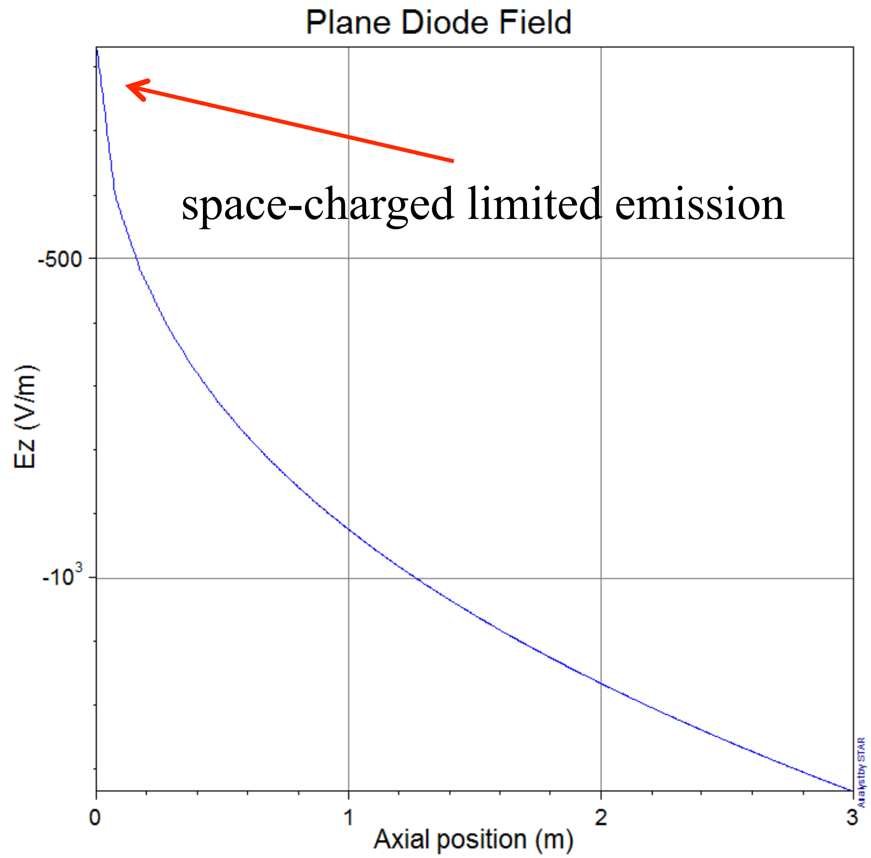

Child-Langmuir current: 133.870 mA

Computed current: 133.874 mA

Relative error:
3 x 10^{-5}

Steady-state current for the CPI gun: comparison with experimental data at 31 kV

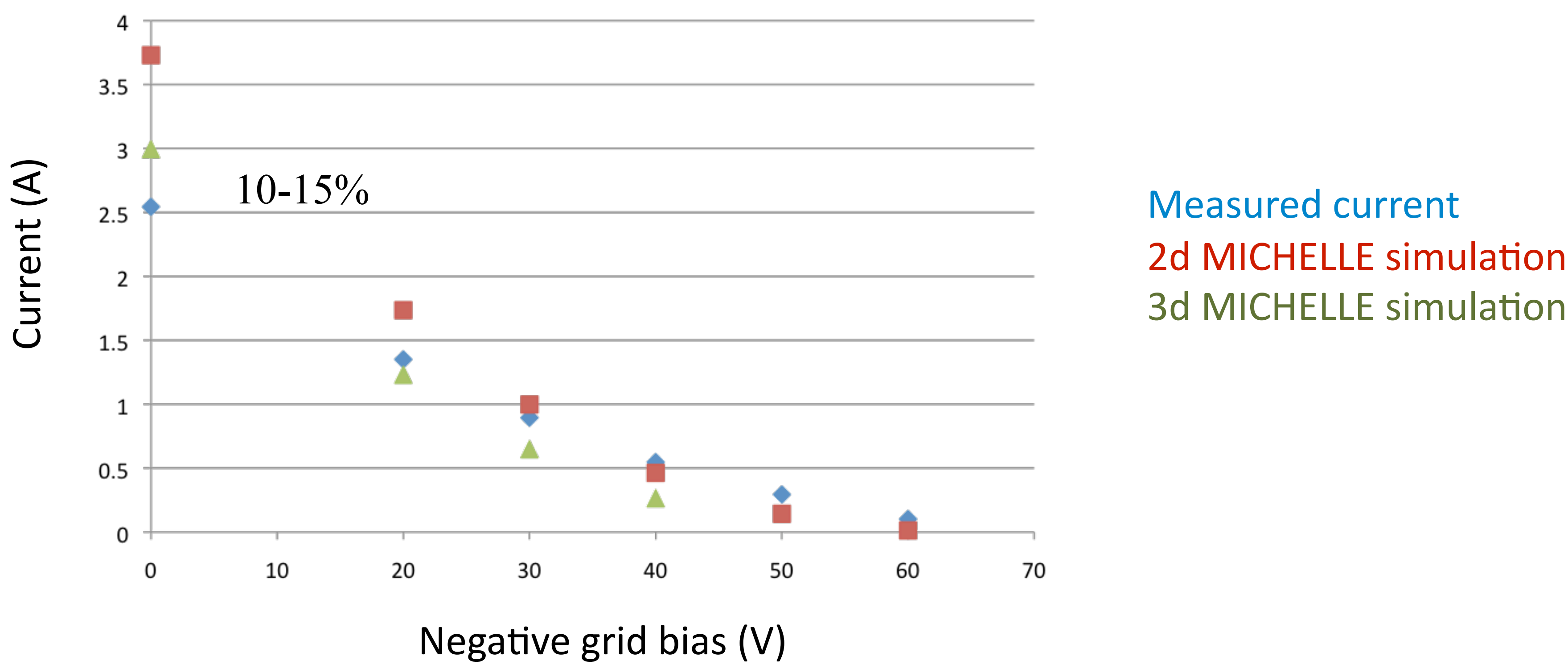

Longitudinal bunching in the gap

Time-dependent current in a plane diode

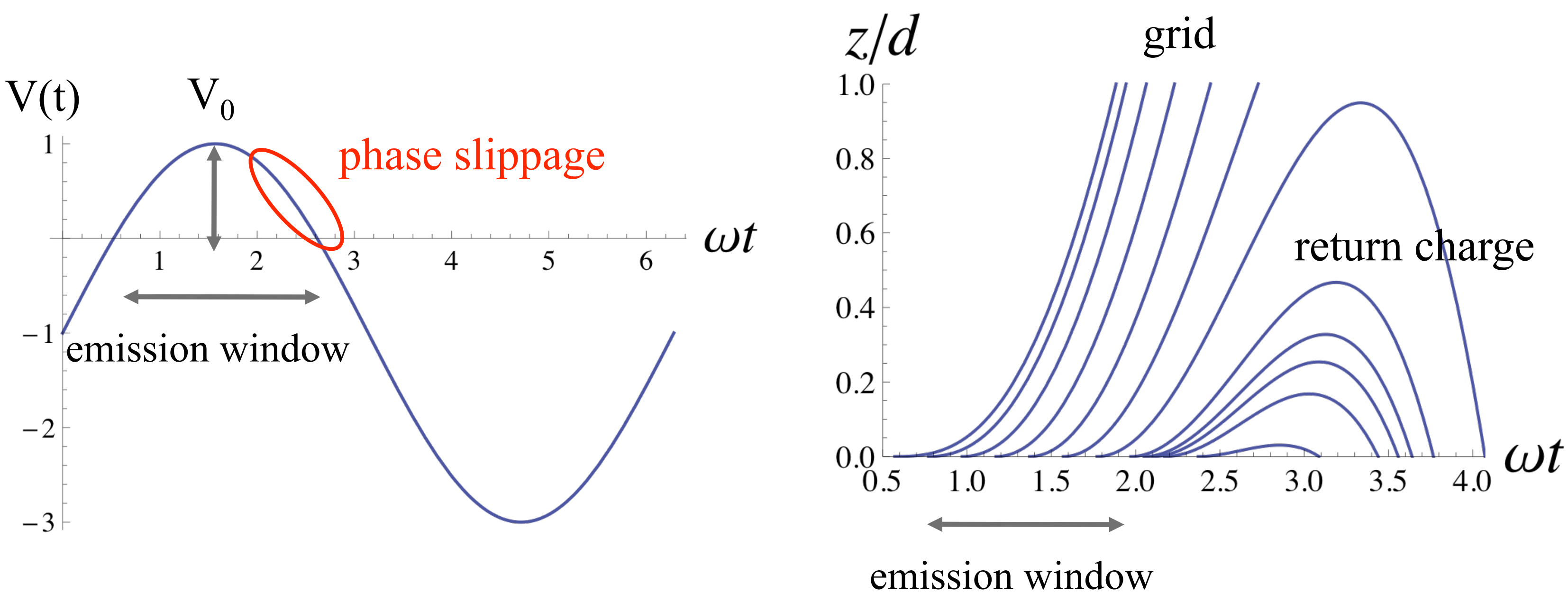

Longitudinal bunching in the gap

Natural time and charge scales

$$T_{CL} = 3L\sqrt{m/2eV_0} \qquad Q_{CL} = \frac{4}{3}\varepsilon_0 V_0 / L$$

- No charge makes it across when: $\Delta T < T_{CL}/2$.
- Asymptotic behavior for $\Delta T > T_{CL}$.
- Describes bunch charge and rms pulse width at the grid.

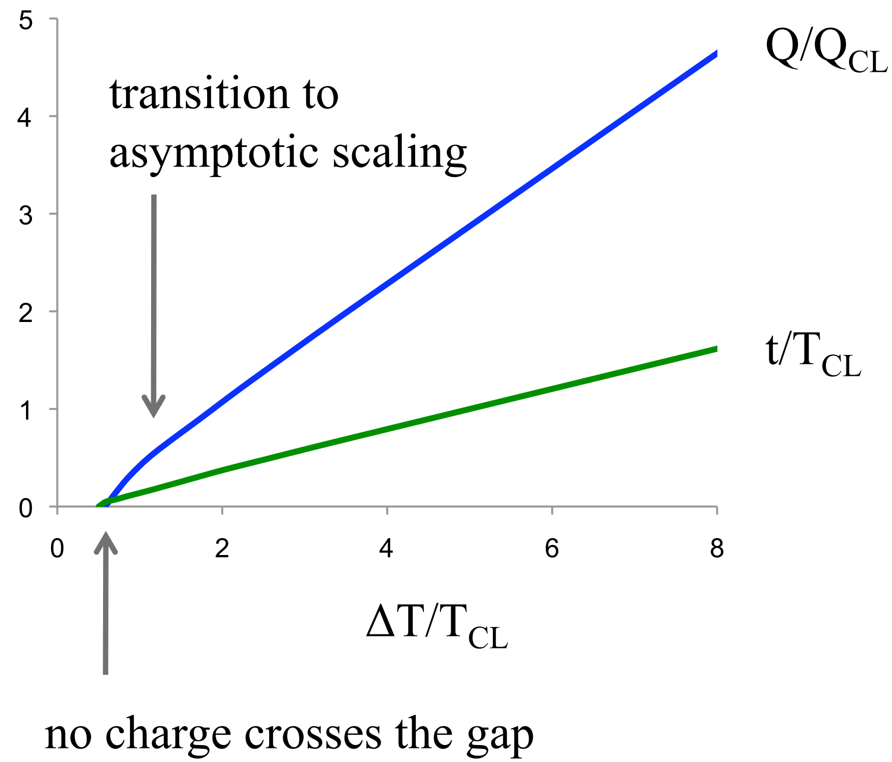

2d Simulation Results

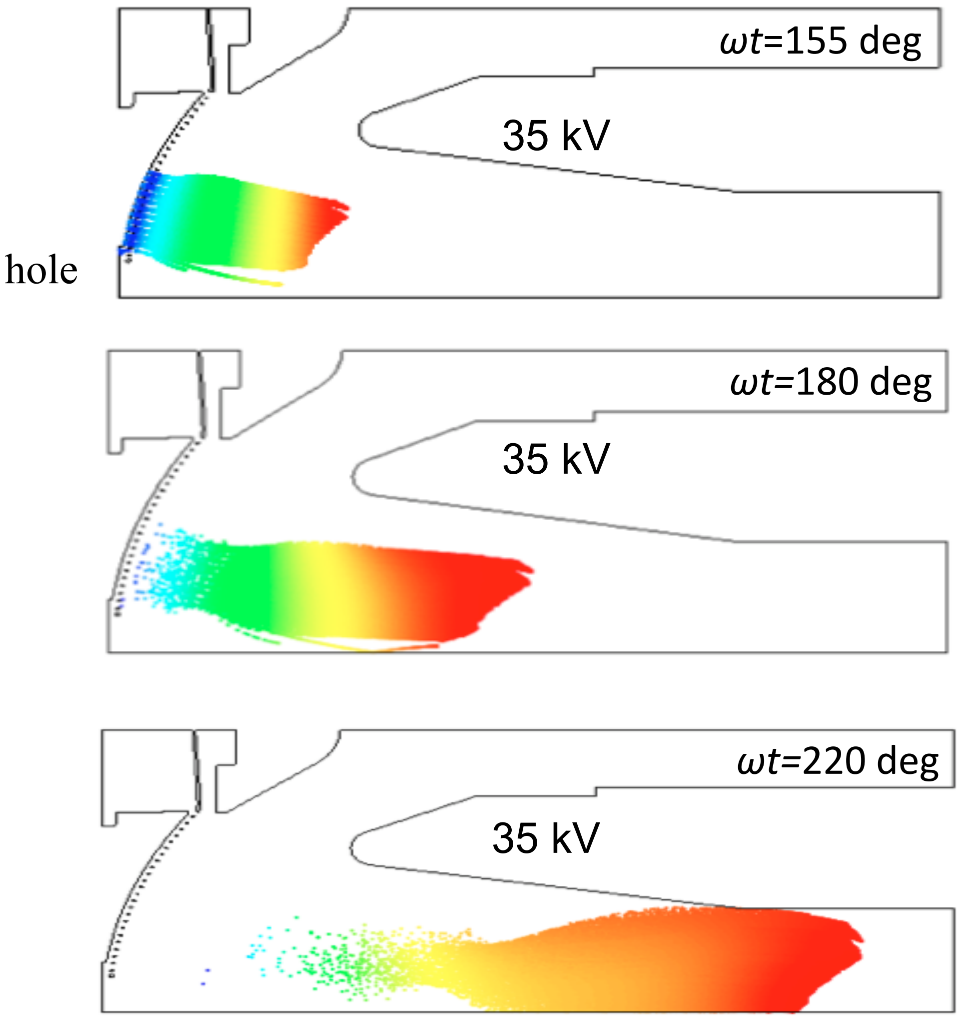

Rep rate: 700 MHz
Charge: 0.9 nC
Average current: 0.6 A
Peak current density: 8.8 A/cm^2

In this simulation, emission is restricted to a portion of the cathode surface.

color denotes values of $\beta_z\gamma$

red – maximum
blue – minimum

Close-up of emission region:

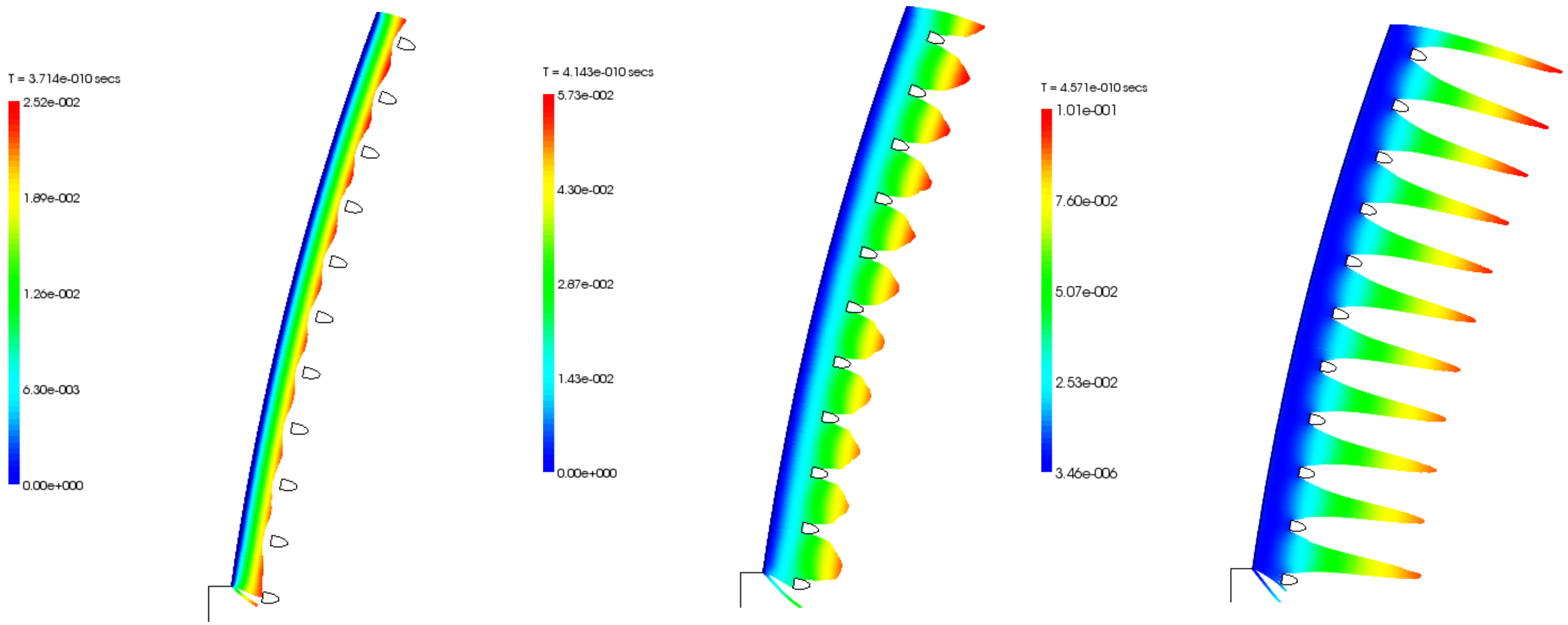

Emission takes place primarily between grid wires due to variations of the field across the cathode surface.

The grid divides the beam into a collection of focusing beamlets.

color denotes values of $\beta_z\gamma$

Phase Space at Gun Exit

Transverse phase space

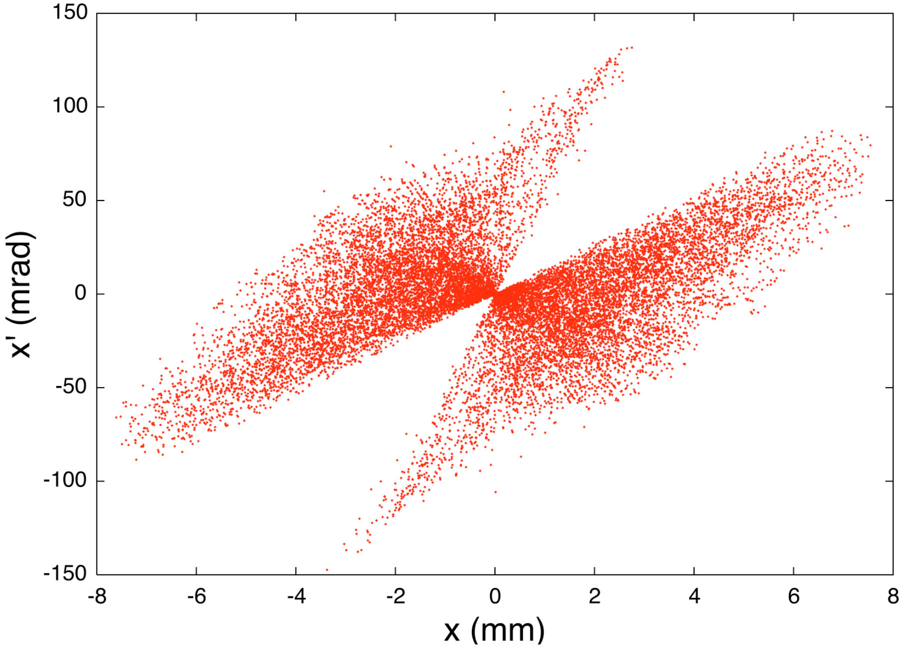

Longitudinal phase space

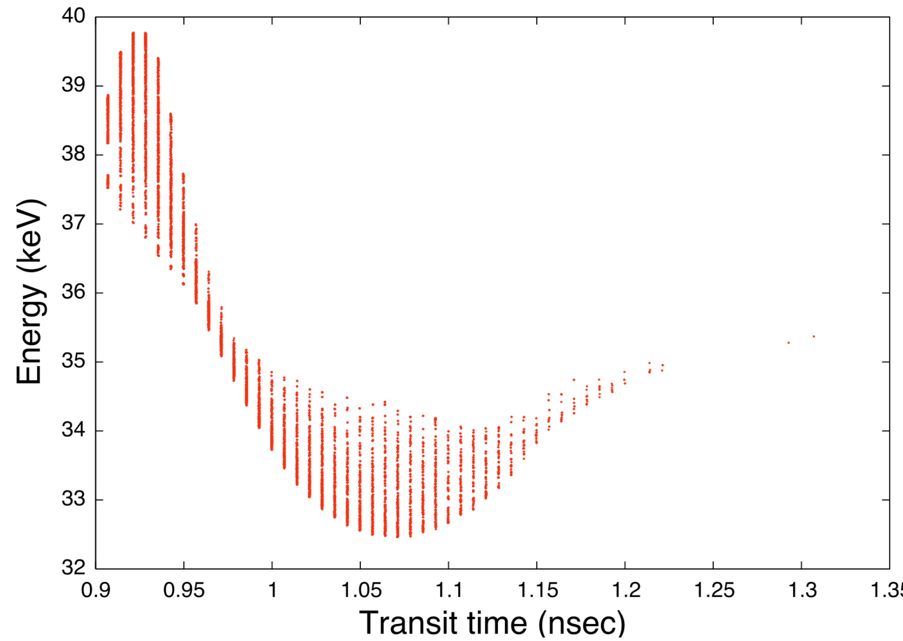

Normalized *x*-emittance: 28 mm-mrad

Normalized *z*-emittance: 20 keV-ps

Bunch radius (rms): 0.43 cm
Bunch duration (rms): 54 psec
Energy spread (rms): 5%

Comparison of 2d and 3d Current Pulses

35 kV, -450 V grid bias, parameters for 0.9 nC bunch

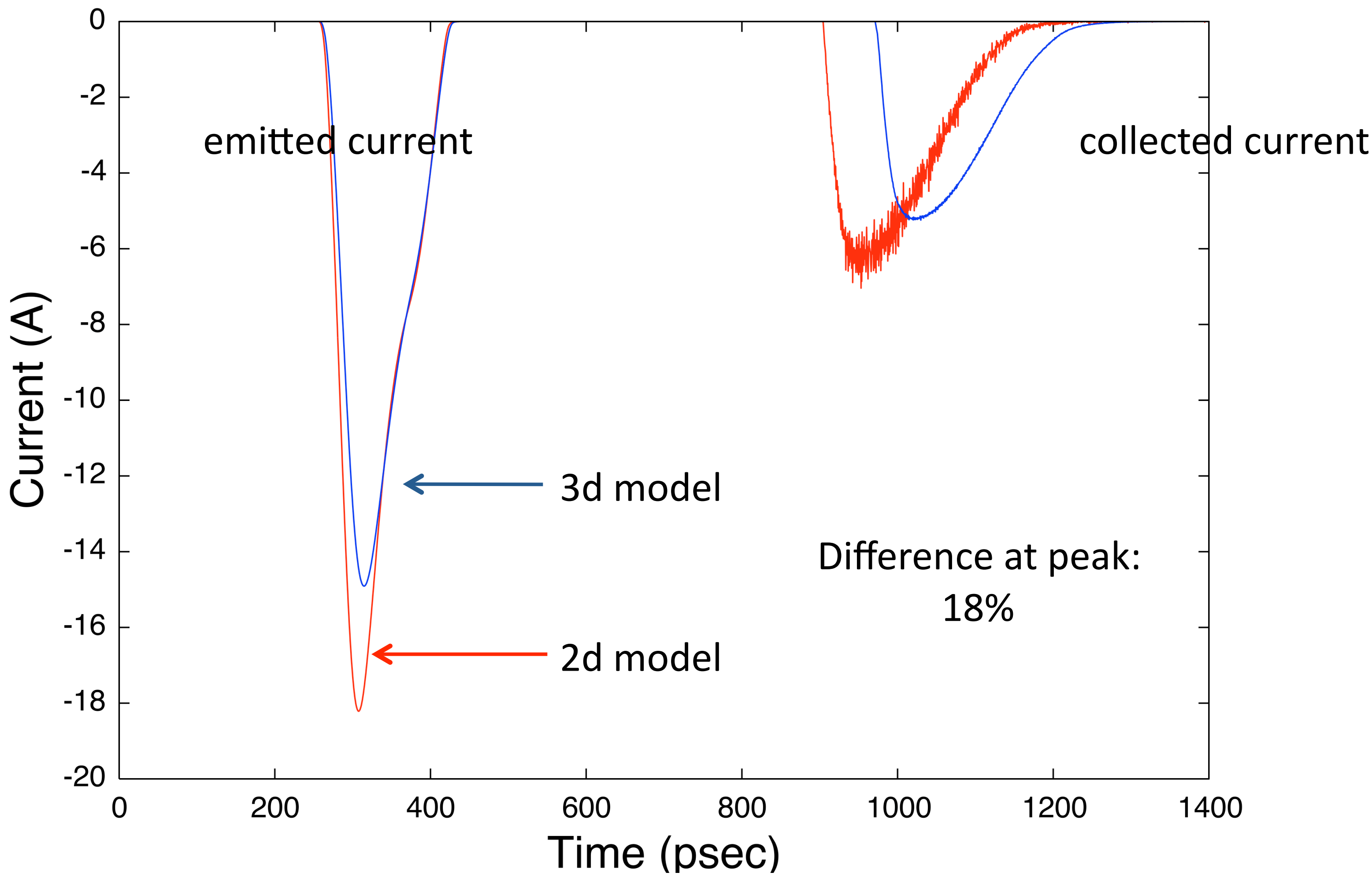

Comparison of 2d and 3d Bunch Diagnostics

2d Simulation		*3d Simulation*
Bunch charge (nC) = 0.88	15%	Bunch charge (nC) = 0.75
Average energy (keV) = 35.147		Average energy (keV) = 35.053
Transit time (nsec) = 0.99372		Transit time (nsec) = 1.0058
xrms (cm) = 0.30181		xrms (cm) = 0.28035
x-Emittance (mm-mrad) = 28.616	2%	x-Emittance (mm-mrad) = 29.156
z-Emittance (keV-ps) = 19.6297		z-Emittance (keV-ps) = 20.8095
RMS dt (psec) = 54.408		RMS dt (psec) = 54.761
RMS dW (keV) = 1.8584		RMS dW (keV) = 1.8037

Good agreement in transverse and longitudinal emittances.

Can transverse emittance be improved?

Sources of Injector Gun Emittance

1. Most emittance growth takes place in the cathode-grid gap.

2. Primary sources of emittance growth include:
   - nonuniformity of the fields near the cathode surface
   - nonlinear scattering fields of the grid wires

3. Reducing emittance due to fields at the cathode surface
   - close the hole in the cathode to eliminate nonlinear fields near the inner radius
   - prevent emission near the outside of the cathode to minimize edge and geometrical effects (overfocusing of outer trajectories)

4. Reducing emittance due to the grid
   - reduce the radius of the beam intercepting the grid
   - increase the energy with which particles intercept the grid
   - decrease the jump in electric field across the grid

Model of Grid Emittance

A kick-map approximation can be used to determine the focusing effect of the grid on each beamlet, producing an expression for the transverse rms emittance.

$$\varepsilon_{x,n} \approx G R_b h \left(\frac{q^2}{2mc^2} \right)^{1/2} \frac{\left| \Delta E_z \right|}{E^{1/2}}$$

emittance of a single slice at time t

G – dimensionless geometrical factor (a function of h/R_b)
R_b – radius of beam intercepting the grid
h – distance between grid wires
ΔE_z – jump in longitudinal electric field across the grid at time t
E – energy of a particle passing between two grid wires at time t

In the steady-state case, $E = qV_g$ where V_g is the potential between two wires.

Steady-State Grid Emittance

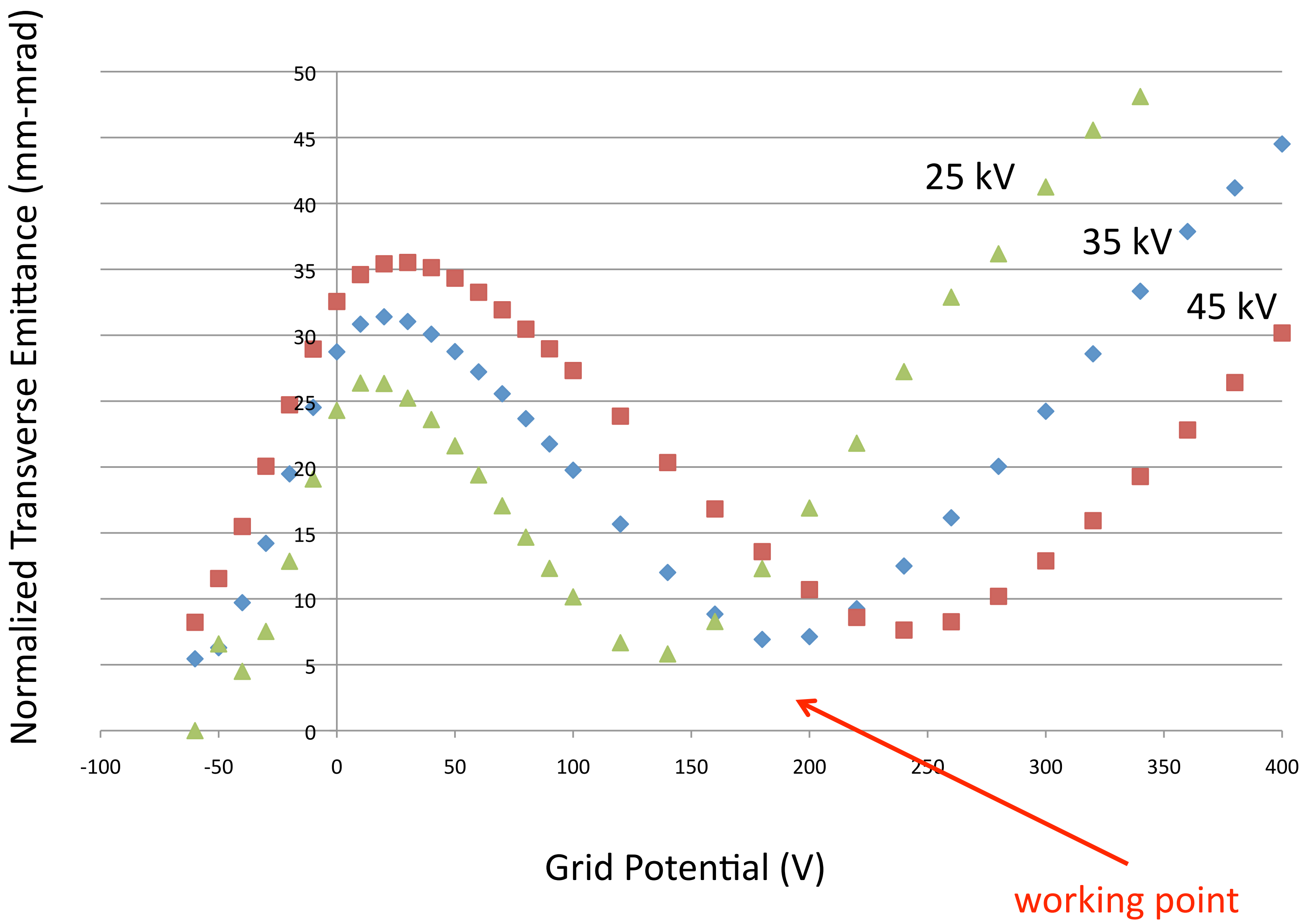

Grid Emittance of a Bunch

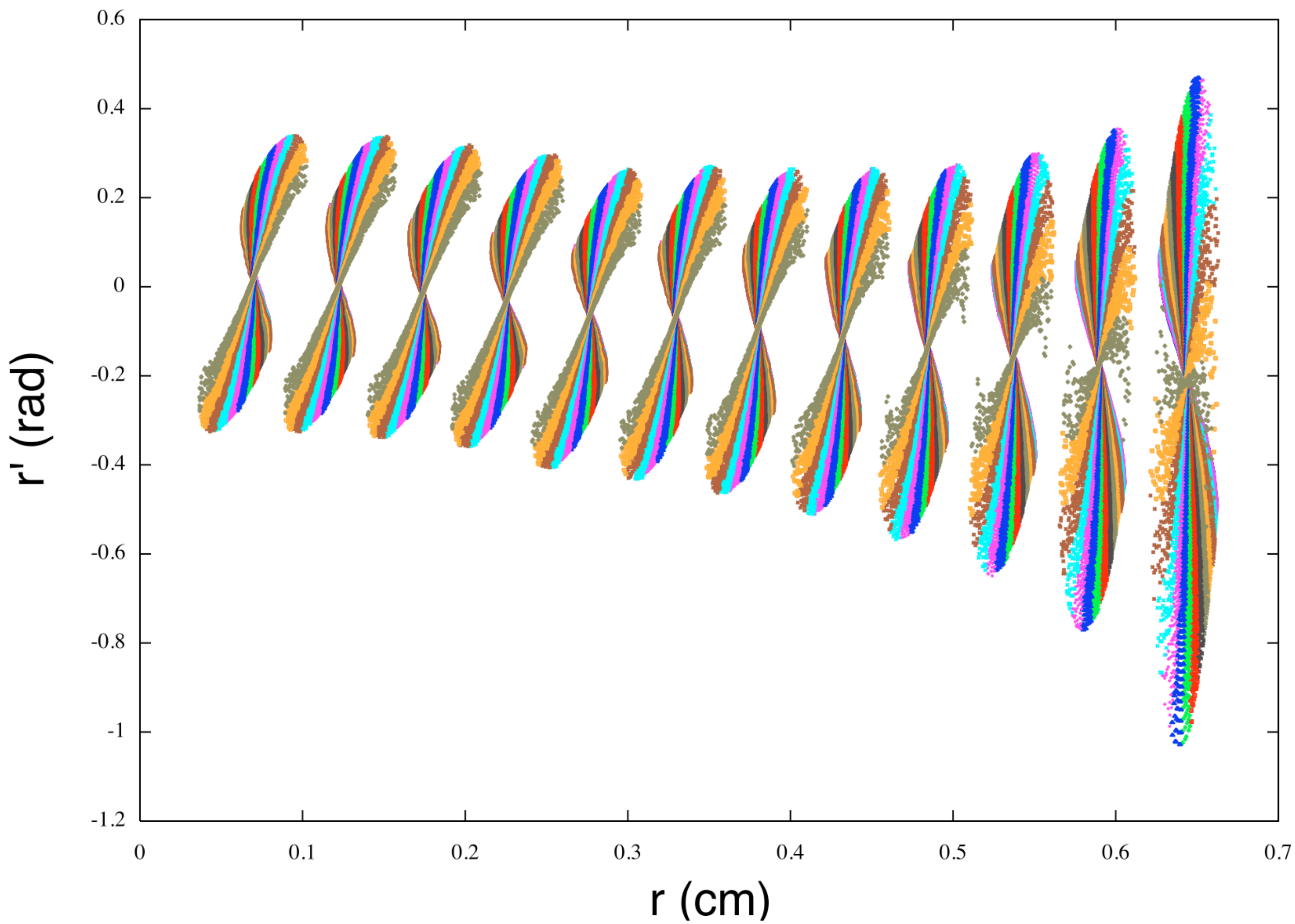

The bunch is divided into slices by crossing time (color).

Each slice receives a different focusing kick from the grid.

Simulation of a Low-Emittance Bunch

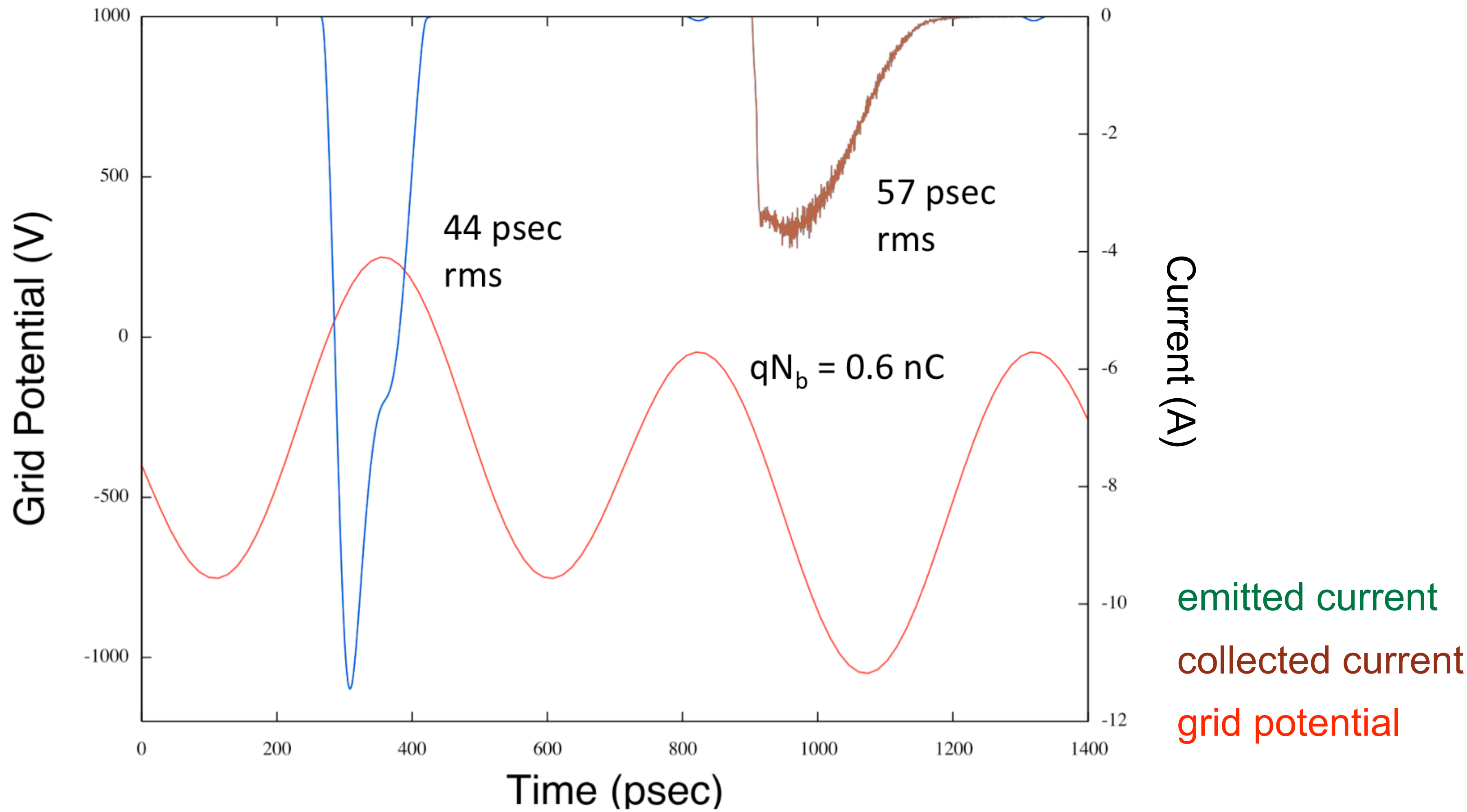

Phase Space for Low-Emittance Bunch Simulation

Transverse phase space

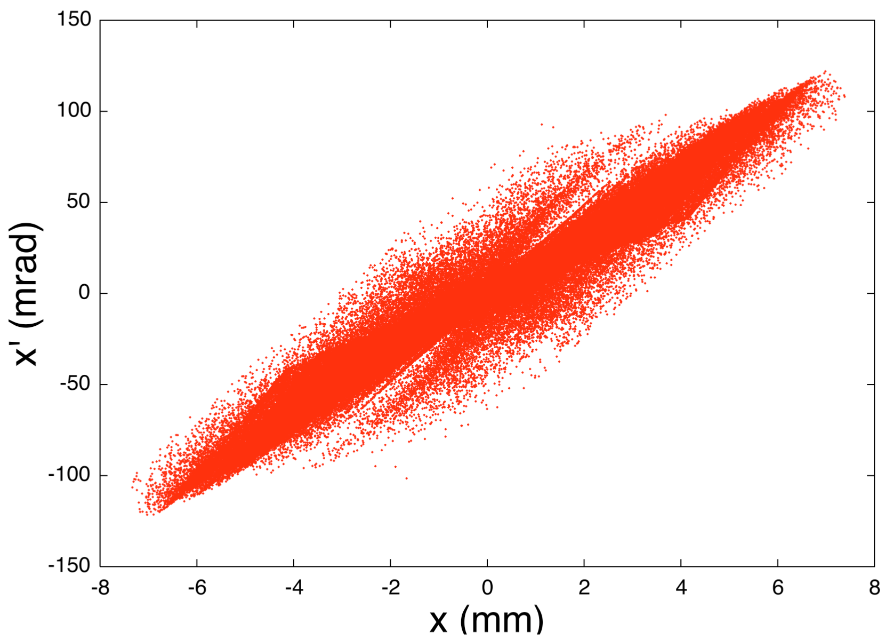

Longitudinal phase space

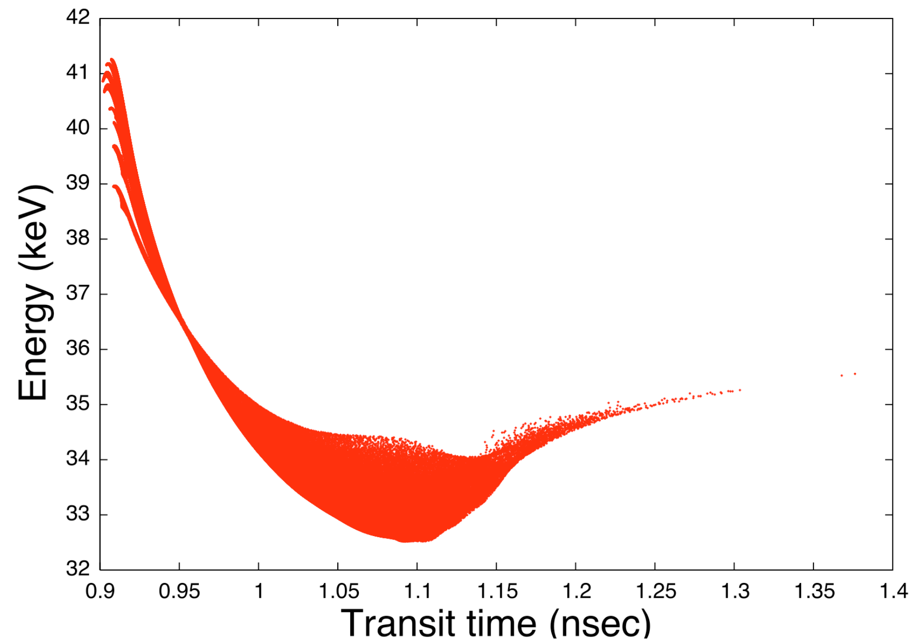

Projected transverse emittance - 8.7 mm-mrad

Projected longitudinal emittance - 21 keV-psec

Summary

- RF-gated thermionic guns can achieve the high rep rate, high average currents, and short bunch lengths necessary for a high average power FEL.
- IOT gun designs are not ideal for producing low emittance bunches. However, emittances < 10 mm-mrad can be obtained if extreme care is taken.
- Benchmarking against experimental results will be underway as results become available.
- Additional work remains to be done to validate 3d simulation results and complete additional design optimization.